

AD A073443

DDC FILE COPY

(12) LEVEL II

TECHNICAL REPORT

TO

THE OFFICE OF NAVAL RESEARCH
CONTRACT NO. N00014-78-C-0275

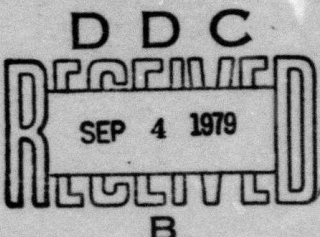
APPLICATION OF RAPID SOLIDIFICATION TECHNIQUES
TO ALUMINUM ALLOYS

BY

R. Mehrabian, C. Levi, S. C. Hsu, S. Kou

Department of Metallurgy and Mining Engineering
Department of Mechanical and Industrial Engineering
University of Illinois
Urbana, Illinois 61801

July, 1979



Sponsored by:
DEFENSE ADVANCED RESEARCH PROJECTS AGENCY
ARPA Order Number: 3517
Effective Date of Contract: 1 February 1978
Contract Expiration Date: 31 January 1980

Reproduction in whole or in part is permitted for any
purpose of the United States Government. Distribution
of this document is unlimited.

DISTRIBUTION STATEMENT A

Approved for public release;
Distribution Unlimited

79 08 28 007

The views and conclusions contained in this document are those of the authors and should not be interpreted as necessarily representing the official policies, either expressed or implied, of the Defense Advanced Research Projects Agency or the U. S. Government.

REPORT DOCUMENTATION PAGE		READ INSTRUCTIONS BEFORE COMPLETING FORM
1. REPORT NUMBER	2. GOVT ACCESSION NO.	3. RECIPIENT'S CATALOG NUMBER
6. TITLE (and Subtitle) Application of Rapid Solidification Techniques to Aluminum Alloys		9. TYPE OF REPORT & PERIOD COVERED Technical Report 1 Feb 78 - 30 Jun 79
7. AUTHOR(s) R. Mehrabian, C. Levi, S. C. Hsu, S. Kou		10. PERFORMING ORG. REPORT NUMBER 15. CONTRACT OR GRANT NUMBER(s) N00014-78-C-0275 X ARPA Order-3517
8. PERFORMING ORGANIZATION NAME AND ADDRESS Department of Metallurgy and Mining Engineering Department of Mechanical and Industrial Engineering University of Illinois, Urbana, IL 61801		
11. CONTROLLING OFFICE NAME AND ADDRESS Dr. E. C. vanReuth Defence Advanced Research Projects Agency 1400 Wilson Blvd., Arlington, VA 22209		
12. REPORT DATE 11. JUL 1979		
13. NUMBER OF PAGES 12 86p		
14. MONITORING AGENCY NAME & ADDRESS (if different from Controlling Office) Dr. B. A. MacDonald, Metallurgy Division Office of Naval Research, Code 471 Department of the Navy Arlington, VA 22217		
15. SECURITY CLASS. (of this report) Unclassified		
15a. DECLASSIFICATION/DOWNGRADING SCHEDULE		
16. DISTRIBUTION STATEMENT (of this Report) DISTRIBUTION STATEMENT A Approved for public release; Distribution Unlimited		
17. DISTRIBUTION STATEMENT (of the abstract entered in Block 20, if different from Report) Approved for public release; Distribution Unlimited		
18. SUPPLEMENTARY NOTES DDC REF ID: A65112 B SEP 4 1979		
19. KEY WORDS (Continue on reverse side if necessary and identify by block number) Rapid Solidification, Surface Melting, Atomization, Heat Flow, Lasers.		
20. ABSTRACT (Continue on reverse side if necessary and identify by block number) This program is being conducted for the purpose of developing a predictive model of heat flow and solidification for aluminum alloys produced under the high cooling rate conditions achievable in atomization and surface melting. It is a combined experimental and theoretical study of the relationship between the important solidification variables (e.g. cooling rate, temperature gradients, interface shape and velocity, supercooling and transformation kinetics) and the structure and microchemistry of rapidly solidified aluminum alloys.		

Block No. 20 (cont'd)

This report covers the theoretical aspects of the investigation to date. The first part addresses the solidification of spherical droplets subjected to high rates of heat extraction achievable in various atomization processes. The second part is concerned with the two-dimensional transient heat flow occurring during rapid surface melting and solidification of a bulk substrate subjected to a high intensity heat flux over a circular region on its bonding surface.

ACCESSION for		
NTIS	White Section <input checked="" type="checkbox"/>	
DDC	Buff Section <input type="checkbox"/>	
UNANNOUNCED <input type="checkbox"/>		
JUSTIFICATION _____		
BY _____		
DISTRIBUTION/AVAILABILITY CODES		
Dist.	Avail.	and/or SPECIAL
A		

HEAT FLOW IN ATOMIZED METAL DROPLETS

by

C. G. Levi and R. Mehrabian*

ABSTRACT

The solidification of spherical droplets with a discrete melting temperature is analyzed using an enthalpy model. Equations describing the cooling of the initially superheated liquid droplet and a numerical heat flow model for its subsequent solidification are presented. Important parameters like times for initiation and completion of solidification, cooling rates and interface velocities in aluminum, iron and nickel are related to the process variables governing the rate of heat extraction from the droplets. The analysis is performed for the range of Biot numbers of practical interest where Newtonian cooling models are not considered applicable, $0.01 \leq Bi \leq 1.0$, and the results are presented in the form of normalized or dimensionless quantities. It is shown that the average cooling rate in the liquid prior to solidification can be computed with the Newtonian cooling expressions. However, significant temperature gradients are noted at the droplet surface even for Biot numbers as low as 0.01. Reducing the droplet diameter reduces the times necessary for the initiation and completion of solidification, increases

*C. G. Levi and R. Mehrabian are Graduate Student in the Department of Metallurgy and Mining Engineering and Professor in the Department of Metallurgy and Mining Engineering and the Department of Mechanical and Industrial Engineering, respectively, University of Illinois, Urbana, IL 61801.

the interface velocities at equivalent fractions solidified and decreases the G_L/R ratio. Although smaller droplet diameters promote higher cooling rates in the liquid at the beginning and in the solid at the end of solidification, the effect at the intermediate stages is more complex and depends on the initial superheat, the Biot number and the thermophysical properties of the material.

I. INTRODUCTION

During solidification of metal powders heat is extracted from the droplets by both convection and radiation at their surface. However, there are no accurately established values for the combined radiative and convective heat transfer coefficient, h , and direct measurement of the cooling rate or heat flux during solidification of an atomized droplet would be extremely difficult, if not impossible. In gas atomization the convective heat transfer coefficient is overriding and an upper limit of $\sim 10^5 \text{ W/m}^2\text{K}$ can be estimated from existing expressions for h under the most favorable experimental conditions (1).

Indirect estimates of heat transfer coefficients in various atomization processes have also been made by comparison of measured segregate (dendrite arm) spacings in crystalline alloy powders with predetermined relationships between these spacings and average cooling rates during solidification. The heat transfer coefficients for gas atomization deduced in this way are of the same order of magnitude as those estimated from mathematical expressions (1).

In general, then, a limitation on the achievable heat transfer coefficient at a liquid metal droplet - environment interface can be translated into a limitation on the important dimensionless variable, Biot number*, governing the rate of heat extraction from the droplet. For example, a heat transfer coefficient $h \leq 10^5 \text{ W/m}^2\text{.K}$ translates to a range of Biot numbers of $10^{-2} \leq Bi \leq 1.0$ for atomized droplets of liquid aluminum in the size range of $1\mu\text{m}$ to $1000\mu\text{m}$.

* see nomenclature

Previous work on modelling the solidification of metal droplets has been either confined to the Newtonian cooling regime or to a specific range of heat transfer coefficients (1-3). In this paper general relationships are developed between the rate of heat extraction and the important solidification parameters, assuming the heat is transferred only by conduction inside a spherical droplet under concentric isotherms. Since Newtonian cooling expressions are considered applicable for Biot numbers below .01 and the limitations on h set an upper limit for Bi of ~ 1.0 , as indicated above, this study is aimed to analyze the heat flow during solidification of superheated metal droplets with Biot numbers within this range.

II. PROBLEM STATEMENT AND SOLUTION APPROACH

We consider the cooling of a superheated pure liquid metal droplet and its subsequent solidification due to radially uniform heat loss by radiation and convection from its surface. Surface conductance - heat transfer coefficient - and the temperature of the environment are assumed to remain constant. The thermal properties of the solid and the liquid are also assumed to be constant, but different. Heat transfer inside the droplet is by conduction only.

First, a dimensionless form of the analytical solution to the one-dimensional heat conduction equation in spherical coordinates is used to determine the temperature profile in the droplet when its surface reaches the melting point. This profile is then used as the initial boundary condition for the subsequent solidification problem. The concepts of the enthalpy model recently proposed by Shamsundar and Sparrow (4) are used to develop the numerical solutions for the solidification portion of the problem. In this model the enthalpy is used as a dependent variable in addition to the temperature, and the finite difference equations are written in a fully implicit form. The important variables during cooling and solidification of the droplets are determined and expressed in their most general dimensionless form over a range of Biot numbers of practical interest for droplets of three elements: aluminum, nickel and iron.

III. MATHEMATICAL DESCRIPTION

For mathematical consistency all the equations in the following formulation are written in terms of the dimensionless Fourier and Biot numbers expressed in terms of the properties of the liquid. The cooling of the liquid droplet prior to solidification was described in terms of the analytical infinite-series solution for the radially uniform cooling of a sphere with a moderate heat transfer coefficient, given in reference (5).

For the solidification part of the problem the spherical droplet is divided into a fixed number of concentric shell domains of thickness Δr for the internal nodes ($2 < i < n$), and $\Delta r/2$ for the center ($i=1$) and the surface ($i = n+1$) nodes. An energy balance for an internal volume element can then be written as:

$$\frac{\partial \left(\frac{H_i - H_S^*}{\Delta H_{SL}} \right)}{\partial \left(\frac{\alpha_L t}{r_0^2} \right)} = - \frac{k^-}{k_S} \frac{r_o a_i^-}{v_i} \left| \frac{\partial \left[\frac{C_S (T - T_M)}{\Delta H_{SL}} \right]}{\partial \left(\frac{r}{r_0} \right)} \right|^- + \frac{k^+}{k_S} \frac{r_o a_i^+}{v_i} \left| \frac{\partial \left[\frac{C_S (T - T_M)}{\Delta H_{SL}} \right]}{\partial \left(\frac{r}{r_0} \right)} \right|^+ \quad (1)$$

where a_i^- , a_i^+ and v_i denote the inner and outer surface areas and the volume of the spherical nodal shell i , respectively. All the variables in equation (1) and those given below are defined in the Nomenclature.

Equation (1) can now be put in terms of dimensionless nodal enthalpy, ψ_i , and dimensionless nodal temperature, θ_i , and becomes:

$$\frac{\alpha_L}{\alpha_S} \frac{\partial \psi_i}{\partial F_0} = \xi_i^+ \left. \frac{\partial \theta}{\partial \phi} \right|_i^+ - \xi_i^- \left. \frac{\partial \theta}{\partial \phi} \right|_i^- \quad (2)$$

$$\text{where: } \xi_i^+ = \frac{k^+}{k_s} \frac{r_o a_i^+}{v_i} \quad (3)$$

$$\xi_i^- = \frac{k^-}{k_s} \frac{r_o a_i^-}{v_i}$$

For the center node, $i = 1$, the second term on the right hand side of equation (2) becomes zero.

For the surface node, $i = n + 1$, an energy balance similar to expression (1) is written which includes heat loss to the environment. Appropriate manipulation of this equation using the definitions of dimensionless nodal enthalpy and temperature yields the following corollary expression to equation (2):

$$\frac{\alpha_L}{\alpha_s} \frac{\partial \psi_{n+1}}{\partial F_o} = - \xi_{n+1}^- \left. \frac{\partial \theta}{\partial \phi} \right|_{n+1}^- - \xi_{n+1}^+ \frac{k_L}{k_s} Bi[\theta_{n+1} + Ste] \quad (4)$$

In general, H_i in equation (1) refers to the specific enthalpy of the volume element i and assumes different forms when the node is in the liquid, the solid or contains the liquid-solid interface. k in equation (3) is the thermal conductivity of the liquid or the solid. $k^+ = k^-$ for all nodes except that containing the interface, $i = \ell$, where $k^+ = k_s$ and $k^- = k_L$.

In the solid region the dimensionless nodal enthalpy, ψ_i is always negative and equal to the dimensionless nodal temperature θ_i , whereas in the superheated liquid region ψ_i is larger than unity. A volume element containing the liquid-solid interface is at the melting point of the metal; therefore the value of ψ_ℓ is equal to the fraction of the volume element ℓ that is in the liquid state, i.e. $0 \leq \psi_\ell \leq 1.0$ and $\theta_\ell = 0$.

Equations (2) and (4) were put into their equivalent finite difference forms using backward difference formulas. The resulting system of simultaneous equations for the different nodes was solved using the Gauss-Seidel iterative method starting with the temperature distribution obtained from the analytical solution for the pre-solidification stage (5). The convergence criteria used for each iteration cycle was:

$$\sum_{i=1}^{n+1} \left| \left(\psi_{i,j+1}^t / \psi_{i,j+1}^c \right) - 1 \right| \leq 10^{-4} \quad (5)$$

where the superscripts *t* and *c* denote the trial and calculated values, respectively.

The dimensionless time interval ΔF_0 was adjusted in every step *j* to give roughly uniform displacements of the liquid-solid interface. Trial runs were performed changing the number of nodes, *n*+1, and the length of the interface displacements, $\Delta\phi^*$, (i.e., the length of the time steps ΔF_0). It was observed that for the metals investigated, increasing the number of nodes above 21 does not significantly affect the results. On the other hand, some parameters, like G_L/R , cooling rates in the liquid $\bar{\Omega}_L$ and interface velocities at the beginning ($\phi^* \rightarrow 1$) and at the end ($\phi^* \rightarrow 0$) of solidification are particularly sensitive to the time step size, especially in the low range of Biot numbers. For these calculations the time step sizes were appropriately selected until convergence was reached. Calculations were performed on a CDC CYBER 175 computer.

IV. RESULTS AND DISCUSSION

The analytical equations and the computer heat flow model were used to calculate the important cooling and solidification parameters (e.g. cooling rates, interface velocities, temperature gradients, etc.) as a function of time and the dimensionless variables -mainly Biot Number- governing the rate of heat extraction from the droplets. The range of Biot numbers investigated cover the values of practical interest in liquid metal atomization where Newtonian cooling models are not considered applicable. Calculations were carried out for droplets of aluminum, iron and nickel, using the thermal and physical properties listed in Table I.

In the first part of this section the results obtained from the analytical solution for the cooling of the liquid are described. Figure 1 shows the dependence of the cooling time, t° , (i.e., time for the surface of the droplet to reach its melting point) on the Biot Number and initial superheat. The time calculated from the analytical solution has been normalized for purposes of representation, dividing it by the time obtained from the Newtonian cooling model, which is:

$$\left. \frac{\alpha_L t}{r_0^2} \right|_{\text{Newt.}} = \frac{\ln (1 + \theta_0/\text{Ste})}{3Bi} \quad (6)$$

As expected, at equivalent initial superheats the time for non-Newtonian cooling is shorter because not all the sensible heat in the droplet is removed before its surface reaches the melting point. Examples of calculated cooling times, t° , from Figure 1

for 50 and 500 μm droplets of Al, Fe and Ni are given in Table II. Note that increasing the particle diameter by one order of magnitude (and hence the Biot number) will increase the cooling time by less than one order of magnitude as indicated by the values in the ordinate of Figure 1, which can be interpreted as correction factors to equation (6).

Normalized temperature distributions in liquid droplets when their surface reaches the melting point, for different Biot Numbers and dimensionless initial temperatures are shown in Figure 2. The largest gradient occurs at the surface and is given by the transformed boundary condition:

$$\frac{\partial}{\partial \phi} \left(\frac{T - T_M}{T_0 - T_M} \right) = Bi \cdot \left(\frac{Ste}{\theta_0} \right) = Bi \cdot \frac{(T_M - T_g)}{(T_0 - T_g)} \quad (7)$$

It should be noted that the actual temperature gradient at the droplet surface is independent of initial superheat and droplet size. Furthermore, calculations show that the effect of superheat on temperature distributions is negligible for $Bi \lesssim 0.01$. However, the results also indicate that even for small Biot numbers, in the range of ~ 0.01 , there may be significant temperature gradients in a metal droplet. For example, in a 20 μm diameter droplet of liquid iron where $Bi \sim 0.01$ ($h = 4 \times 10^4 \text{ W/m}^2\text{K}$) the maximum temperature gradient -at the droplet surface- when $t = t^\circ$ is $\sim 1.5 \times 10^6 \text{ K/m}$ and a temperature difference of 7.5 K between the surface and the center of the droplet was calculated from the analytical solution.

Thus, the Newtonian cooling assumption that temperature differences inside a body are negligible for $Bi \leq 0.01$ may not always be justified. Other examples of gradients at the surface of various droplets are given in Table II.

An important variable affecting supercooling prior to nucleation is the cooling rate in a liquid droplet. The instantaneous average cooling rate $\bar{\Omega}$ estimated from the series-type solution was found to be identical to that obtained from the Newtonian cooling approximation. When the surface of the droplet reaches its melting point ($t = t^o$) the cooling rate is:

$$\bar{\Omega}_L^o = \frac{\alpha_L}{r_0^2} \frac{\Delta H_{SL}}{C_S} (3 \cdot Bi \cdot Ste) = \frac{3 \alpha_L (T_M - T_g)}{k_L} \cdot \frac{h}{r_0} \quad (8)$$

Examples of the calculated cooling rates for $50\mu\text{m}$ and $500\mu\text{m}$ droplets of Al, Fe and Ni assuming a high heat transfer coefficient of $5 \times 10^4 \text{ W/m}^2 \text{ K}$ are given in Table II.

The next part of this section contains the results obtained from the computer simulation of heat flow during solidification using the temperature distributions shown in Figure 2 as initial conditions.

The net solidification time for droplets of Al, Fe and Ni as a function of Biot number and dimensionless initial superheat is presented in Figure 3. The time resulting from the numerical solution of the enthalpy model has been normalized dividing it by the time calculated from the following expression for solidification in a Newtonian regime:

$$\left. \frac{\alpha_L t_f}{r_0^2} \right|_{\text{Newt.}} = [3 \text{ Bi Ste } (C_L/C_S)]^{-1} \quad (9)$$

As anticipated, increasing initial superheat prolongs solidification, and the effect is larger as the Biot Number increases; the sensible heat retained in the liquid portion of the droplet increases resulting in longer times from initiation to completion of solidification. For example, 500 μm droplets of Fe solidifying with an $h = 5 \times 10^4 \text{ W/m}^2\text{K}$ ($\text{Bi} = 0.31$) will require $4.8 \times 10^{-3} \text{ s}$ to complete solidification with no initial superheat and $5.3 \times 10^{-3} \text{ s}$ with a dimensionless initial superheat of 0.1 ($\sim 150\text{K}$), see Table II. The effect of superheat on net solidification times diminishes with decreasing Biot Numbers.

Figure 4 shows dimensionless liquid-solid interface velocities as a function of Biot Number for various positions of the interface in Al droplets solidifying with concentric isotherms. The data show that dimensionless interface velocity increases with Biot Number and the progress of solidification.

The dimensionless interface velocity for Newtonian solidification is:

$$\left. \frac{r_0}{\alpha_L} R \right|_{\text{Newt.}} = \left(\frac{1}{\phi^*} \right)^2 \text{ Bi Ste } \frac{C_L}{C_S} \quad (10)$$

For a given interface position, ϕ^* , equation (10) would give a straight line with a slope of unity in Figure 4. The ratio of calculated non-Newtonian to Newtonian interface velocities is

close to unity in the beginning of solidification for the case of no superheat regardless of Biot number. On the other hand, this ratio decreases with increasing fraction solid and increasing Biot number at a given fraction solid. In general, increasing initial superheat in the non-Newtonian regime results in a corresponding decrease in solid-liquid interface velocities. However, this effect is only noticeable in the initial stages of solidification, and decays rapidly with increasing superheat and decreasing Biot number.

Examples of calculated interface velocities are given in Table II. Note that during non-Newtonian solidification increasing the particle size by one order of magnitude (without changing h) reduces the actual interface velocity at a particular fraction solid; On the other hand, increasing the heat transfer coefficient h (without changing r_0) will increase R at any location.

The results of normalized ratio of temperature gradient in the liquid at the liquid-solid interface, G_L , to interface velocity R for the three metals and a dimensionless initial superheat θ_0/Ste of 0.3 are presented in Figure 5. G_L at the beginning of solidification is given by the boundary condition at the surface:

$$G_L \Big|_{\phi^*=1} = \frac{1}{r_0} \text{Bi Ste} \cdot \frac{\Delta H_{SL}}{C_s} \quad (11)$$

while the initial interface velocity is close to that calculated

from equation (10), hence, the initial G_L/R ratio should asymptotically approach a constant value with decreasing Biot number:

$$\left. \frac{G_L}{R} \right|_{\phi^*=1} \rightarrow \frac{\Delta H_{SL}}{\alpha_L C_L} \text{ when } Bi \rightarrow 0 \quad (12)$$

Examples of G_L/R ratios calculated from Figure 5 are listed in Table II. As expected, this parameter decreases rapidly with the progress of solidification, and with Biot number for a given position of the liquid-solid interface. Furthermore, reduction of the initial superheat (not shown in Figure 5) results in a corresponding decrease in G_L/R , the effect being more pronounced when θ_0/Ste is in the range of 0 to 0.1.

Normalized values of the calculated average cooling rates in the solid and the liquid during solidification of iron droplets are shown in Figures 6 and 7, respectively. Note that the part of the normalizing factor inside the brackets is the Newtonian net solidification time obtained from equation (9), which is directly proportional to r_0 and inversely proportional to h . Therefore, increasing the Biot number by increasing the droplet size, r_0 , will increase the actual cooling rate only if the slope of the curve at that point is larger than unity. On the other hand, increasing the heat transfer coefficient h will always increase the cooling rate.

The average cooling rate in the solid, $\bar{\eta}_S$, Figure 6, increases with the progress of solidification for $Bi \lesssim 0.9$. However, the results also indicate that for higher Biot numbers the cooling rate has a maximum at some intermediate stage during solidification, ($\phi^* \neq 0$). Finally, decreasing the initial superheat will always increase the achievable cooling rates in the solid, but the effect is only felt at the initial stages of solidification.

The average cooling rate in the liquid, $\bar{\Omega}_L$, for iron, Figure 7, decreases with the progress of solidification; the effect being more pronounced at small Biot numbers.

Examples of average cooling rates $\bar{\Omega}_S$ and $\bar{\Omega}_L$ calculated from Figures 6 and 7 and similar plots obtained for aluminum and nickel (showing identical trends) are given in Table II.

SUMMARY

The infinite series analytical solution to the cooling of an initially superheated metal droplet under concentric isotherms was coupled to a numerical solution for the heat flow problem during the subsequent solidification, written in terms of both enthalpy and temperature as dependent variables. The results obtained from this analysis as compared to those predicted by the Newtonian cooling model for aluminum, iron and nickel are summarized below:

- 1) Both models predict that the average cooling rate in the liquid prior to solidification, $\bar{\Omega}_L^\circ$, is directly proportional to the heat transfer coefficient, h , inversely proportional to the droplet radius r_0 , and independent of initial superheat.
- 2) The cooling time (for the surface to reach the melting point), t° , estimated from the analytical solution increases with increasing superheat towards the Newtonian model prediction (which is a logarithmic relationship). Reducing r_0 has a less pronounced effect on t° than the direct proportionality indicated by the Newtonian model. On the other hand, increasing h has a more pronounced effect on decreasing t° than the inverse proportionality predicted by the Newtonian expression.
- 3) Substantial temperature gradients at the surface of the droplet when $t = t^\circ$ are calculated from the analytical solution for Biot numbers as low as 0.01. Although these gradients are independent of superheat, the latter markedly influences the internal temperature profiles for $Bi \geq 0.01$.
- 4) Reducing r_0 diminishes the net solidification time, t_f , in a more pronounced way than the direct proportionality predicted by the Newtonian model. Furthermore, it increases the interface

velocity R at equivalent fractions solidified towards the values predicted by the Newtonian model (which are independent of r_0). Reducing r_0 also decreases the G_L/R ratios and increases the achievable cooling rates in the liquid $\bar{\Omega}_L$ at the beginning of solidification, $\phi^* \rightarrow 1$, and in the solid $\bar{\Omega}_S$ at the end of it, $\phi^* \rightarrow 0$. The effect of r_0 on $\bar{\Omega}_L$ and $\bar{\Omega}_S$ at intermediate stages during solidification is more complex and depends on the metal, the corresponding Biot numbers and the initial superheat, as well as the fraction solidified.

- 5) Increasing h reduces t and increases R in a less pronounced manner than that predicted by the Newtonian model. It always increases G_L/R as well as the cooling rates $\bar{\Omega}_L$ and $\bar{\Omega}_S$ at any stage during solidification. The progress of solidification always increases the interface velocity and decreases G_L/R as well as cooling rates in the liquid. However, the cooling rate in the solid increases monotonically with time at the smaller Biot numbers but apparently shows a maximum before the end of solidification above a certain Biot number, which for iron is ~ 0.9 and for aluminum and nickel is above 1.0.
- 6) Increasing initial superheat increases t_f , G_L/R and $\bar{\Omega}_L$, but decreases R and $\bar{\Omega}_S$. The effects of superheat are mostly felt in the initial stages of solidification and decay rapidly with decreasing Biot number.

19

NOMENCLATURE

Dimensioned variables

a_i	area of the inner (-) or outer (+) boundary surface of the shell element i
c	specific heat
G_L	gradient in the liquid at the liquid-solid interface
h	heat transfer coefficient at the droplet surface
H	specific enthalpy
H_S^*	specific enthalpy of the solid at T_M (reference value).
ΔH_{SL}	heat of fusion
k	thermal conductivity
r	position along the radial coordinate, $0 \leq r \leq r_0$.
r_0	radius of the spherical droplet
R	interface velocity
t	time
t^*	cooling time
t_f	net solidification time
T	temperature
$T_G = 300^\circ K$	temperature of the cooling medium
T_0	initial temperature of the droplet, $T_0 \geq T_M$
T_M	melting temperature
v_i	volume of the shell element i
$\alpha = k/\rho c$	thermal diffusivity
$\bar{\Omega}$	instantaneous average cooling rate
$\bar{\rho}$	density, average of liquid and solid at T_M

Dimensionless variables

$$Bi = hr_0/k_L$$

Biot number

$$F_0 = \alpha_L t / r_0^2$$

Fourier number (or time)

$$\Delta F_0 = \alpha_L \Delta t / r_0^2$$

time increment

$$Ste = C_S (T_M - T_G) / \Delta H_{SL}$$

Stefan number

$$\phi = r / r_0$$

position

$$\phi^* = r^* / r_0$$

fractional position of the liquid-solid interface

$$\Delta \phi = \Delta r / r_0$$

nodal spacing

$$\phi_i^-, \phi_i^+$$

radius of the surfaces at $r_i - \Delta r/2$ and $r_i + \Delta r/2$, respectively, for the center node $\phi_i^- = 0$ and for the surface node $\phi_{n+1}^+ = 1$.

$$\theta = C_S (T - T_M) / \Delta H_{SL}$$

temperature

$$\theta_0 = C_S (T_0 - T_M) / \Delta H_{SL}$$

initial temperature

$$\theta_0 / Ste$$

superheat

$$\psi = (H - H_S^*) / \Delta H_{SL}$$

enthalpy

Subscripts

f = denotes completion of solidification
 i = nodal index, $1 \leq i \leq n + 1$, $i=1$ for $r=0$, $i=n+1$ for $r=r_0$
 j = time step index, $j \geq 1$
 l = index of volume element containing the liquid-solid interface
 n = number of space intervals between nodes

G = denotes gas environment
 L = liquid
 M = denotes melting
 S = solid

Superscripts

$+$ in the positive r direction
 $-$ in the negative r direction
 $*$ liquid-solid interface
 $^\circ$ denotes the moment when the surface reaches the melting temperature and solidification starts

ACKNOWLEDGEMENT

This research was sponsored by the Defense Advanced Research Projects Agency and was monitored by the Office of Naval Research under Contract Number N00014-78-C-0275. Technical monitor of the contract was Dr. B. A. MacDonald. Partial support for C. Levi through a scholarship from the Consejo Nacional de Ciencia y Tecnologia of Mexico is gratefully acknowledged.

LIST OF REFERENCES

1. R. Mehrabian: RAPID SOLIDIFICATION PROCESSING: PRINCIPLES AND TECHNOLOGIES, p. 9, ed. by R. Mehrabian, B. H. Kear and M. Cohen, Claitor's Publishing Division, Baton Rouge, LA, 1978.
2. M. R. Glickstein, R. J. Patterson II and N. E. Shockley, *Ibid*, p. 46.
3. J. Szekely and R. J. Fisher, *Met. Trans.*, 1970, Vol. 1, pp. 1480-82.
4. N. Shamsundar and E. M. Sparrow, *Jo. of Heat Transfer, Trans. ASME, Series C*, 1975, Vol. 97, pp. 333-40.
5. V. S. Arpaci: CONDUCTION HEAT TRANSFER, p. 288, Addison-Wesley, 1966.

LIST OF FIGURE CAPTIONS

Figure 1 Normalized time for the surface of a liquid droplet to cool from an initial temperature of T_0 to its melting temperature T_M by convection to an environment with constant temperature T_G , as a function of the Biot number and dimensionless initial superheat θ_0/Ste .

Figure 2 Normalized temperature distributions in a liquid droplet when its surface reaches the melting temperature T_M , for different Biot numbers and dimensionless initial superheats $\theta_0/\text{Ste} = (T_0 - T_M)/(T_M - T_G)$.

Figure 3 Normalized net solidification time for liquid droplets of aluminum, iron and nickel, as a function of Biot number and dimensionless initial superheat θ_0/Ste . The calculated curve for nickel with no superheat closely follows that of aluminum for $\theta_0 = 0.3\text{Ste}$.

Figure 4 Dimensionless liquid-solid interface velocity during solidification of aluminum droplets, as a function of Biot number and fractional position of the interface ϕ^* .

Figure 5 Normalized ratio of the temperature gradient in the liquid at the liquid-solid interface, G_L , to the interface velocity, R , during solidification of Al, Fe and Ni droplets, as a function of Biot number and fractional position of the interface. θ_0 and Ste denote the dimensionless initial temperature and Stefan number, respectively.

Figure 6 Normalized instantaneous average cooling rate in the solid during solidification of iron droplets, as a function of Biot number and fractional position of the solid-liquid interface ϕ^* . θ_0 and Ste denote the dimensionless initial temperature and Stefan number, respectively.

Figure 7 Normalized instantaneous average cooling rate in the liquid during solidification of iron droplets, as a function of Biot number and fractional position of the solid-liquid interface $\phi^* = r^*/r_0$. θ_0 and Ste denote the dimensionless initial temperature and Stefan number, respectively.

TABLE I

PROPERTIES OF METALS USED IN THE CALCULATIONS*

Properties	Al	Fe	Ni
Melting Temperature T_M (K)	933	1810	1726
Heat of Fusion ΔH_{SL} (J/Kg) $\times 10^{-5}$	3.95	2.72	3.02
Average Density $\bar{\rho}$ (Kg/m ³) $\times 10^{-3}$	2.46	7.19	8.07
Specific Heat (J/Kg K) $\times 10^{-3}$			
Liquid C_L	1.09	0.787 [†]	0.734
Solid C_S	1.19	0.764 [†]	0.619 [†]
Thermal Conductivity (W/mK)			
Liquid k_L	90.8	40.3	39.3 [†]
Solid k_S	210.8	34.6	87.0 [†]
Thermal Diffusivity $\alpha = k/\bar{\rho}C$ (m ² /s) $\times 10^{+5}$			
Liquid α_L	3.40	0.712	0.664
Solid α_S	7.18	0.630	1.74
Stefan Number (for $T_G = 300K$)	1.91	4.24	2.93
Actual Superheat, $T_0 - T_M$ (K) for			
Dimensionless $\theta_0/\text{Ste} = \frac{T_0 - T_M}{T_M - T_G}$	0.4	253	604
	0.3	190	453
	0.2	127	302
	0.1	63	151
			143

* Thermophysical properties at T_M

† Estimated by extrapolation

TABLE II. CALCULATED SOLIDIFICATION PARAMETERS FOR METAL DROPLETS[†]

METAL	ALUMINUM	IRON	NICKEL
Droplet Diameter, $2r_0$ (μm)	50	50	50
Biot Number, hr_0/k_L	0.014	0.14	0.031
Cooling Time, t^* , (s), for $\theta_0 = 0.1$ Ste the Superheat Indicated $\theta_0 = 0.3$ Ste	4.1×10^{-5} 1.1×10^{-4}	3.1×10^{-4} 1.1×10^{-3}	8.4×10^{-5} 2.4×10^{-4}
Maximum gradient in the Liquid at t^* , (K/m)	3.5×10^5	1.9×10^6	1.8×10^6
Average cooling rate in the liquid, $\dot{\theta}_L$ (K/s), at t^*	1.4×10^6	1.4×10^5	1.6×10^5
Net solidification time, $t_f(s)$ for the superheat indicated $\theta_0 = 0$	2.6×10^{-4} 2.6×10^{-4}	3.2×10^{-3} 3.1×10^{-3}	2.7×10^{-4} 2.6×10^{-4}
Interface velocities, $R(m/s)$ for the interface position indicated. $\theta_0 \leq 0.3$ Ste	4.1×10^{-2} 1.3×10^{-1} 0.1	4.0×10^{-2} 1.0×10^{-1} 4.4×10^{-1}	4.7×10^{-2} 1.1×10^{-1} 4.7×10^{-1}
G/R ratio (K/s/m ²) for the interface position indicated [§]	2.2×10^7 0.9 0.7	4.3×10^7 7.4×10^4 -	1.6×10^8 3.6×10^4 -
Average cooling rate in the liquid $\dot{\theta}_L$ (K/s) for the interface position indicated [§]	7.3×10^5 2.2 0.7	1.1×10^5 1.2×10^3 1.2	1.1×10^6 9.4×10^2 -
Average cooling rate in the solid $\dot{\theta}_S$ (K/s) for the interface position indicated [§]	2.2×10^5 2.4×10^5 1.3×10^6	5.3×10^3 6.1×10^4 1.2×10^5	1.2×10^5 8.7×10^4 1.5×10^5

[†] Assuming $h = 5 \times 10^4$ W/m²
[§] $\theta_0 = 0.3$ Ste

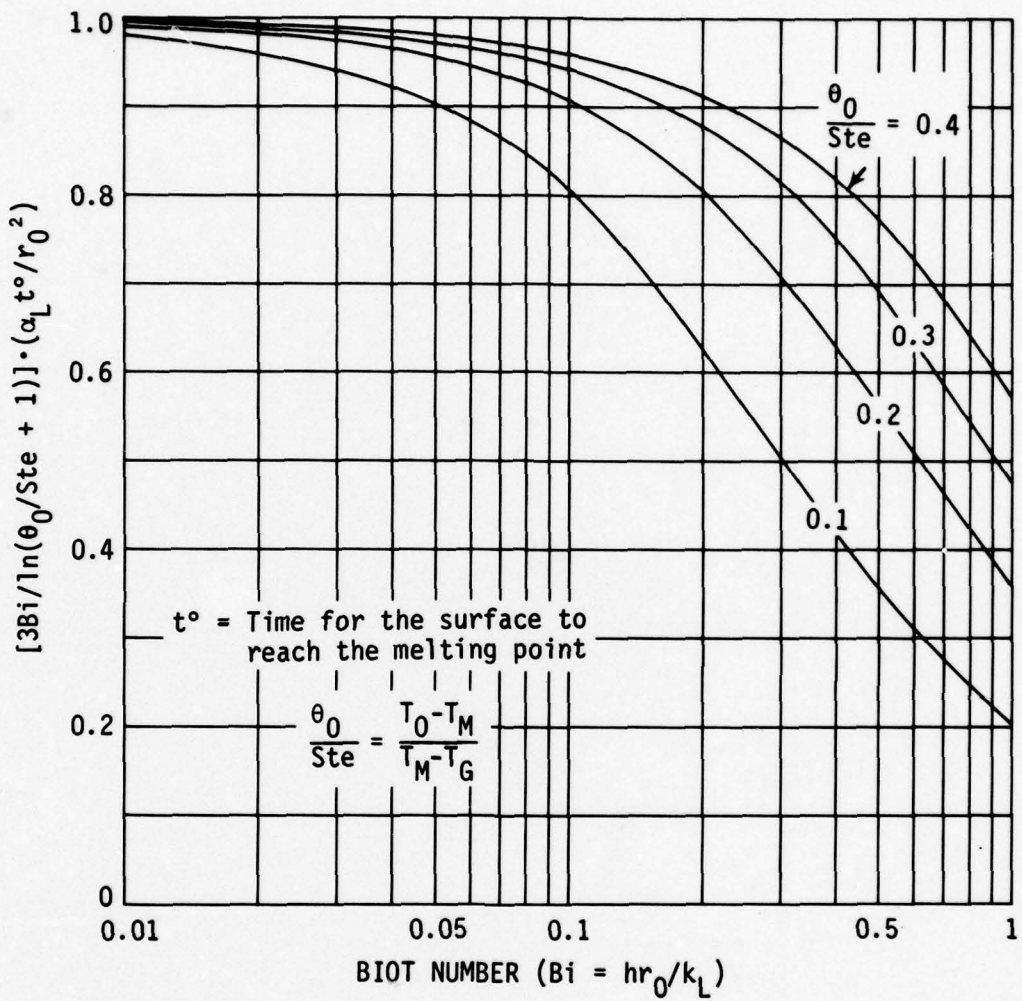


Figure 1. Normalized time for the surface of a liquid droplet to cool from an initial temperature of T_0 to its melting temperature T_m by convection to an environment with constant temperature T_g , as a function of the Biot number and dimensionless initial superheat θ_0/Ste .

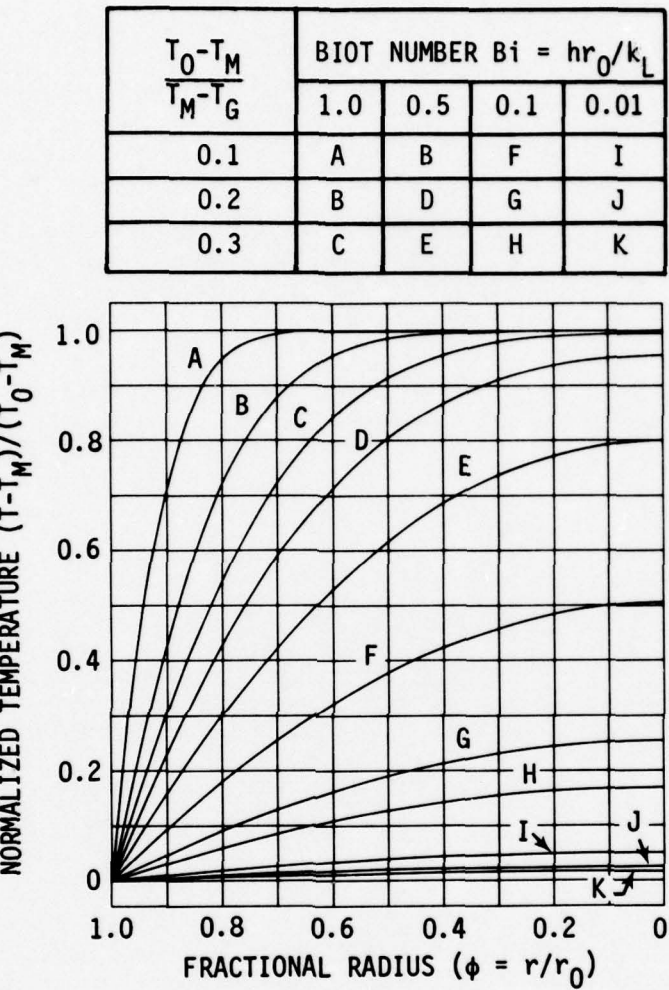


Figure 2. Normalized temperature distributions in a liquid droplet when its surface reaches the melting temperature T_M , for different Biot numbers and dimensionless initial superheats $\theta_0/Ste = (T_0 - T_M)/(T_M - T_G)$.

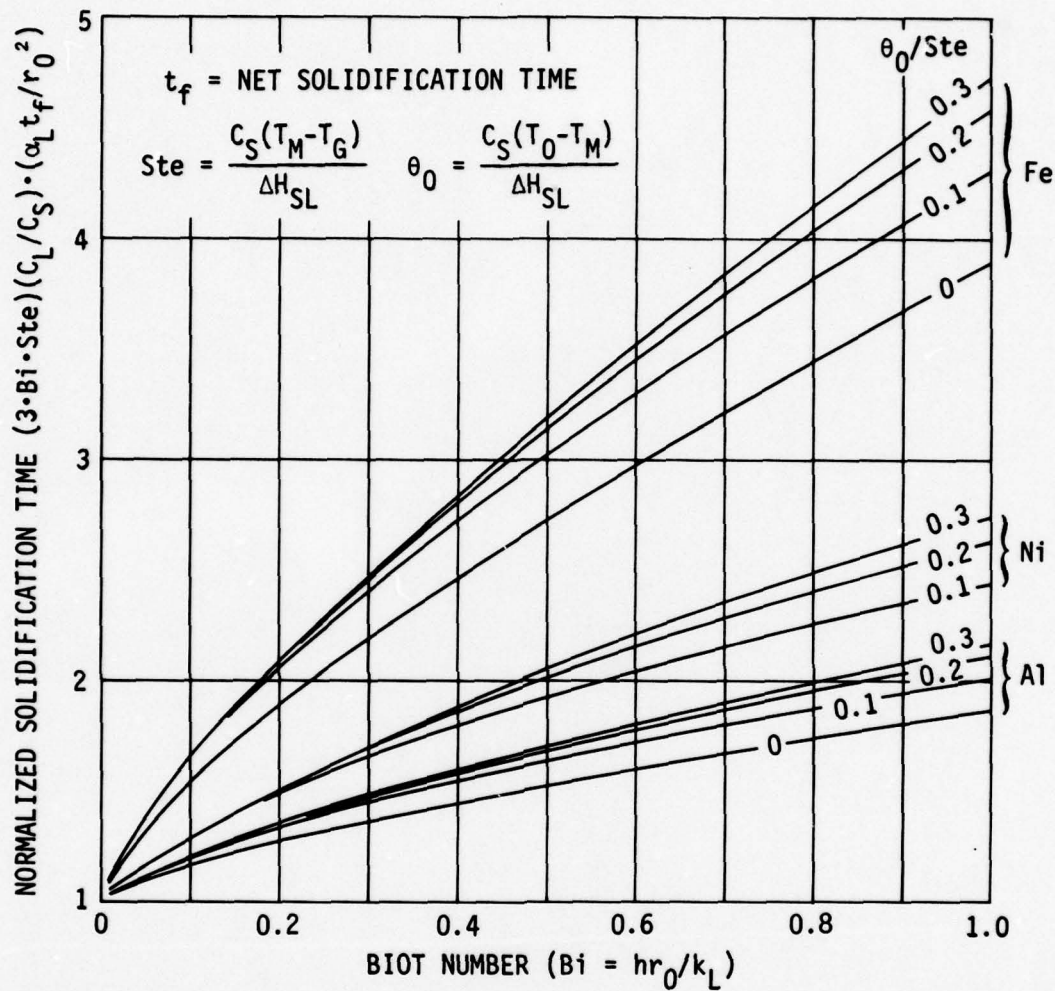


Figure 3. Normalized net solidification time for liquid droplets of aluminum, iron and nickel, as a function of Biot number and dimensionless initial superheat θ_0 / Ste . The calculated curve for nickel with no superheat closely follows that of aluminum for $\theta_0 = 0.3 Ste$.

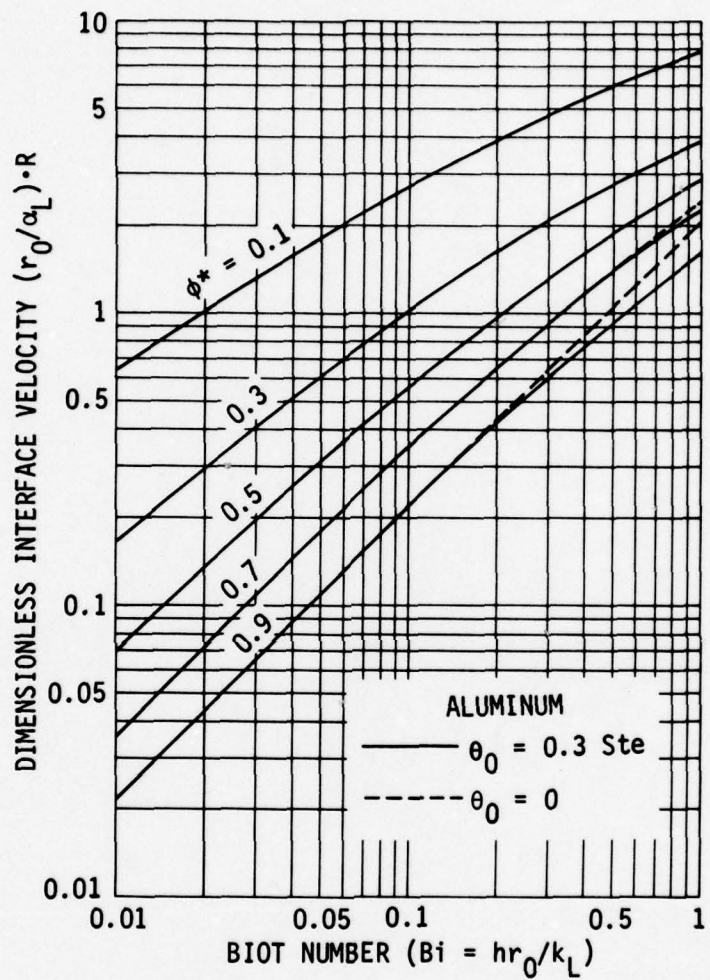


Figure 4. Dimensionless liquid-solid interface velocity during solidification of aluminum droplets, as a function of Biot number and fractional position of the interface ϕ^* .

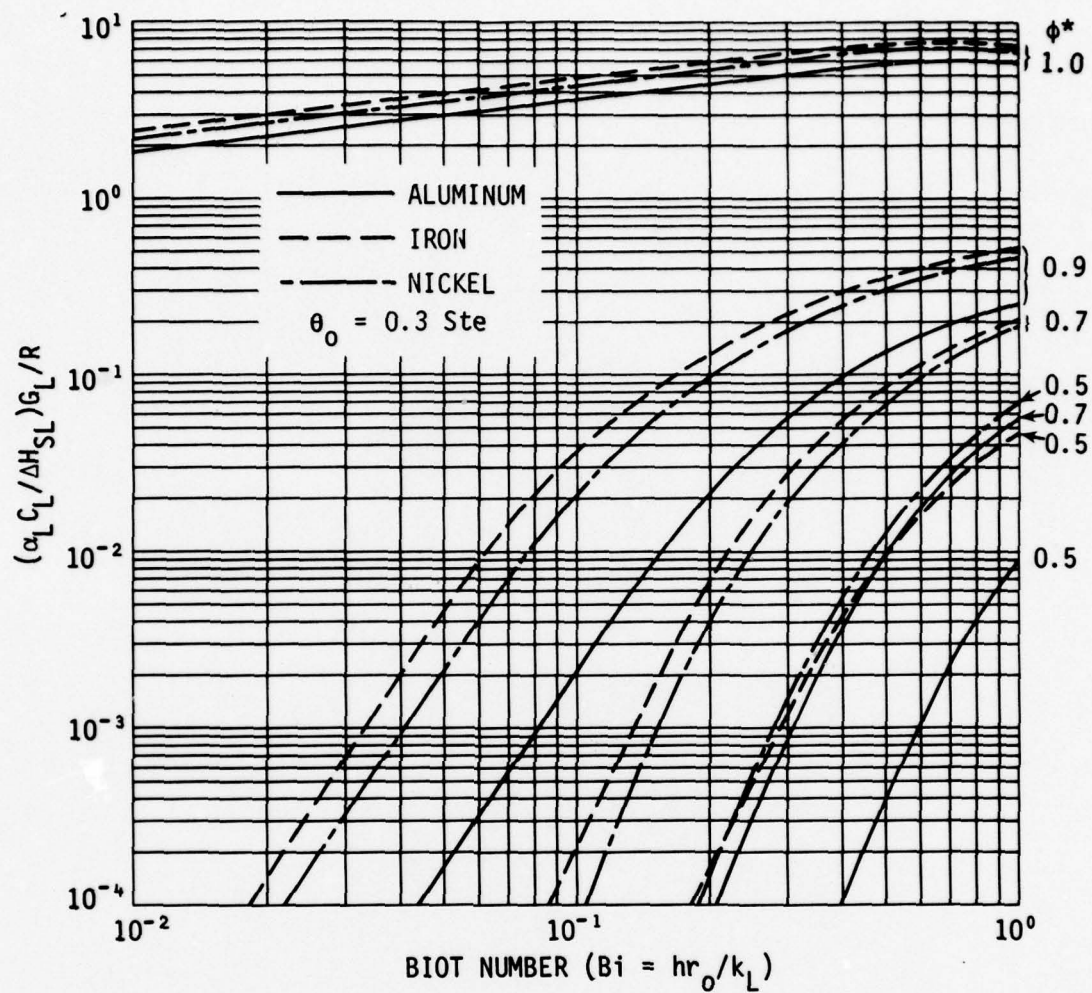


Figure 5. Normalized ratio of the temperature gradient in the liquid at the liquid-solid interface, G_L , to the interface velocity, R , during solidification of Al, Fe and Ni droplets, as a function of Biot number and fractional position of the interface θ_0 and Ste denote the dimensionless initial temperature and Stefan number, respectively.

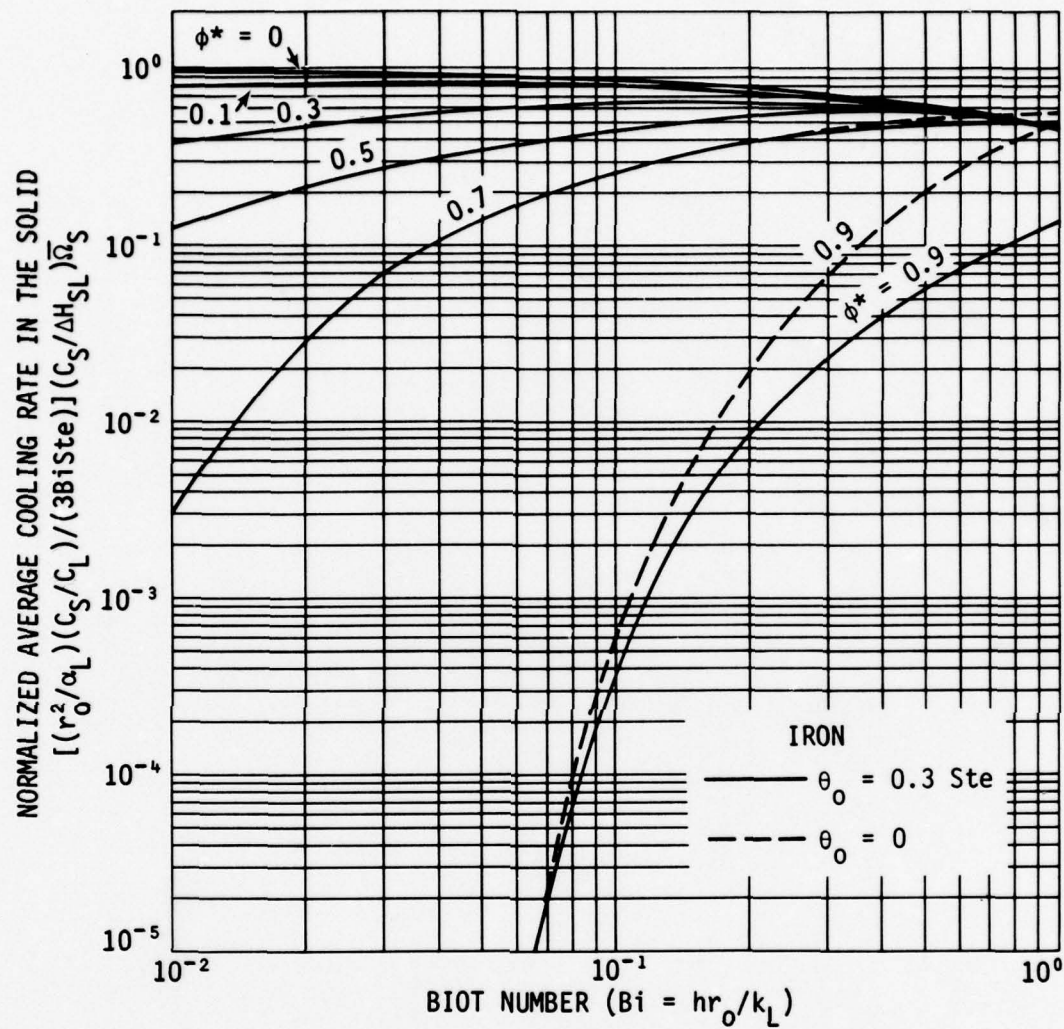


Figure 6. Normalized instantaneous average cooling rate in the solid during solidification of iron droplets, as a function of Biot number and fractional position of the solid-liquid interface ϕ^* . θ_0 and Ste denote the dimensionless initial temperature and Stefan number, respectively.

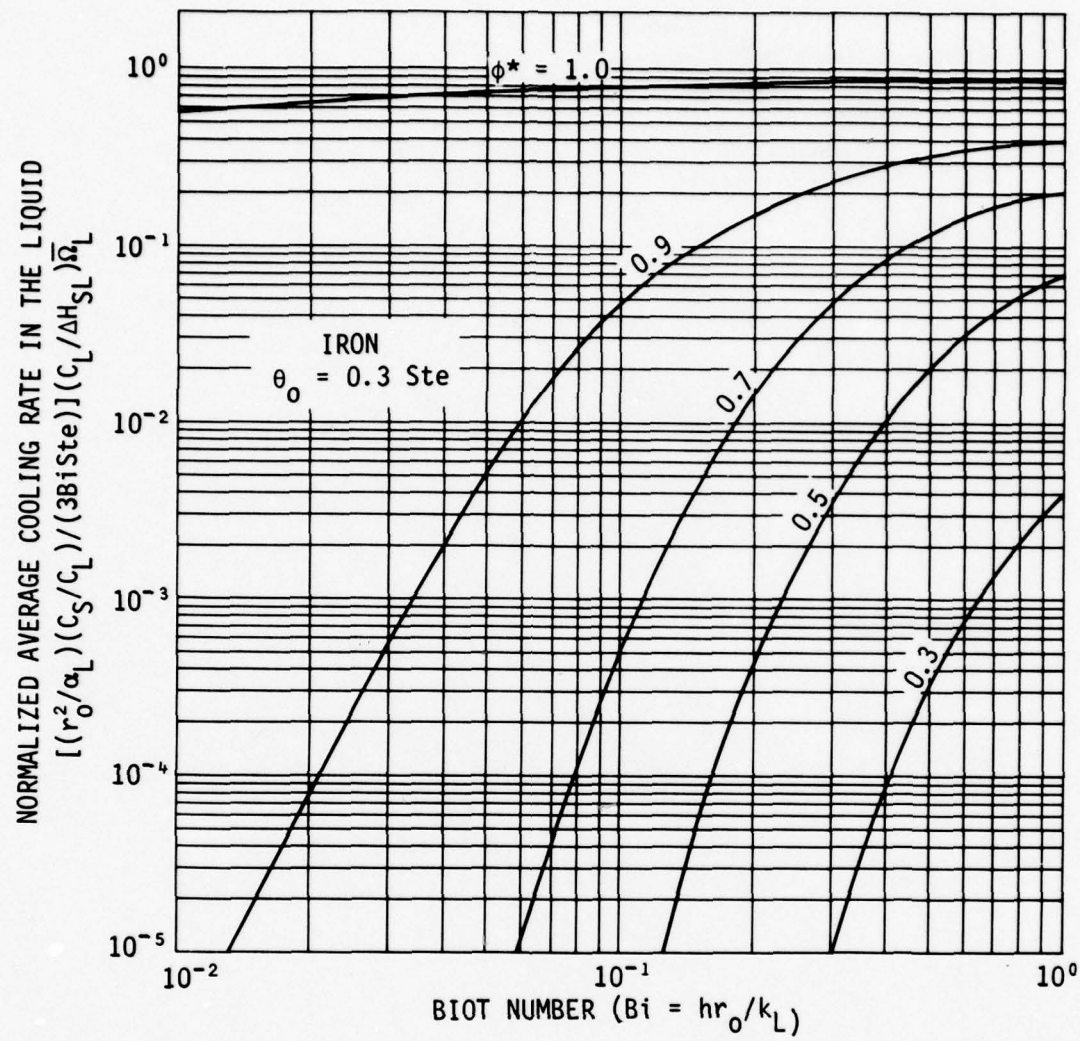


Figure 7. Normalized instantaneous average cooling rate in the liquid during solidification of iron droplets, as a function of Biot number and fractional position of the solid-liquid interface $\phi^* = r^*/r_0$. θ_0 and Ste denote the dimensionless initial temperature and Stefan number, respectively.

RAPID MELTING AND SOLIDIFICATION OF A SURFACE
DUE TO A STATIONARY HEAT FLUX

by

S. C. Hsu, S. Kou and R. Mehrabian*

ABSTRACT

A general two-dimensional computer heat flow model is developed in an oblate spheroidal coordinate system for rapid melting and subsequent solidification of the surface of a semi-infinite solid subjected to a high intensity heat flux over a circular region on its bounding surface. Generalized numerical solutions are presented for an aluminum substrate subjected to both uniform and Gaussian heat flux distributions. Temperature distributions, melt depth and geometry, and melting and solidification interface velocities are calculated as a function of applied heat flux, radius of the circular region, and time. It is shown that the important melting and solidification parameters are a function of the product of the absorbed heat flux, q , and the radius of the circular region, a . General trends established show that melt depth perpendicular to the surface is inversely proportional to the absorbed heat flux for a given temperature at the center of the circular region. Dimensionless temperature distributions and the ratio of liquid-solid interface velocity to absorbed heat flux, R/q , as a function of

*S. C. Hsu formerly, Graduate Research Assistant, Department of Mechanical and Industrial Engineering, University of Illinois is now with G.T.E. Laboratories in Waltham, Mass. S. Kou, formerly Research Associate, Department of Metallurgy and Mining Engineering, University of Illinois is now at the General Motors Research Center, Warren, Michigan. R. Mehrabian is Professor in the Department of Metallurgy and Mining Engineering and the Department of Mechanical and Industrial Engineering, University of Illinois, Urbana-Champaign, Illinois.

dimensionless melt depth remain the same if the product qa is kept constant, while q and a are varied. For a given total power, absorbed melting and solidification parameters are compared for uniform and Gaussian heat flux distributions. For a given temperature at the center of the circular region both melt depth and width are smaller for the Gaussian distribution while temperature gradients and interface velocities are larger.

I. INTRODUCTION

In a recent paper rapid melting and solidification of a metallic surface layer subjected to high intensity heat fluxes, such as those achieved via continuous CO_2 laser radiation, was discussed (1). The effect of absorbed heat flux on the important surface layer melting and subsequent solidification variables of three substrate materials; aluminum, iron and nickel were determined using a simplified one-dimensional computer heat flow model. A second limitation imposed on the previous problem statement was that only uniform heat fluxes were considered. In general, both of these restrictions are violated in practice. Exception is noted for cases where the spot diameter of the incident radiation is large relative to the heat affected zone in the work piece and the one-dimensional heat flow model for the case of uniform heat flux is applicable.

This paper addresses the two-dimensional (axi-symmetric) heat flow problem of the melting and subsequent solidification of a surface layer subjected to a stationary high intensity heat flux over a circular region on its boundary surface. A general method for the solution of this type of a problem is developed which permits treatment of both uniform and non-uniform heat flux distributors in the circular region. Results of numerical computations carried out on a Control Data CYBER 175 computer are presented for a pure aluminum substrate subjected to both uniform and Gaussian heat flux distributors.

The two main assumptions of this paper are: (a) thermal properties of the liquid and the solid are independent of temperature, but different from one another, and (b) convection in the liquid region is not taken into consideration.

II. PROBLEM STATEMENT AND SOLUTION APPROACH

Consider the rapid melting and subsequent solidification of the surface layer of a semi-infinite solid, initially at room temperature, subjected to a high intensity heat flux over a circular region on its bounding surface. The surface outside the heated region is considered adiabatic. The heat conduction equation for the axi-symmetric system is put in oblate spheroidal coordinates which is a "more natural" coordinate system for this problem geometry, i.e., is more compatible with the bounding surface. This results in reduced storage requirements as well as computational time. The generalized expressions derived by Yovanovich et al (2) for the determination of the coefficients in the finite difference equations governing the heat transfer within the discretized spatial domain are used. However, in contrast to previous treatments of melting and solidification problems the finite difference equations are rewritten in terms of the enthalpy model recently proposed by Shamsundar and Sparrow (4) for multi-dimensional phase change problems. In this model the enthalpy is used as a dependent variable in addition to the temperature. In this way a single energy conservation equation is used for each discretized spatial domain which by appropriate substitution of physical constants is applicable regardless of whether the domain is in the liquid state, the solid state or contains the liquid-solid interface. The interface shape, its velocity and other important melting and solidification parameters are obtained by performing auxiliary computations. Finally, the computational technique utilized is a fully implicit one.

III. MATHEMATICAL DESCRIPTION

The axi-symmetric oblate spheroidal coordinate system used in this study is shown in Figure 1. The relationships between the circular cylinder and the oblate spheroidal coordinates are:

$$r = a \cosh n \sin \xi \quad (1)$$

$$z = a \sinh n \cos \xi$$

where a is the radius of the circular region subjected to the heat flux.

The control volume is centered about an arbitrary point (i,j) in space in Figure 1, where i and j indicate the finite discretization of space in the n and ξ directions, respectively. The change in respective coordinate values between successive nodes in the n and ξ directions are Δn and $\Delta \xi$, respectively.

The general formulation of the finite difference representation of the heat conduction equation in orthogonal curvilinear coordinates and its specific form in the discretized domain of Figure 1 centered about node (i,j) is given by Yovanovich et al (2,3). For the specific problem at hand this equation can be put in the following backward difference form:

$$\begin{aligned} -c_1 (T_{i,j}^m - T_{i-1,j}^m) + c_2 (T_{i+1,j}^m - T_{i,j}^m) - c_3 (T_{i,j}^m - T_{i,j-1}^m) \\ + c_4 (T_{i,j+1}^m - T_{i,j}^m) + \frac{P\Delta V}{2\pi k_s r_{i,j} \Delta \xi \Delta n} = \\ \frac{\cosh^2 n_j - \sin^2 \xi_j}{\Delta F_0} (T_{i,j}^m - T_{i,j}^{m-1}) \end{aligned} \quad (2)$$

Where the coefficients are:

$$c_{1,2} = \frac{1}{\Delta n^2} \mp \frac{\tanh n_j}{2\Delta n} \quad (3)$$

$$c_{3,4} = \frac{1}{\Delta \xi^2} \mp \frac{\cot \xi_j}{2\Delta \xi}$$

$$\Delta F_0 = \frac{k_s \Delta t}{\rho C_{ps} a^2} = \frac{\alpha_s \Delta t}{a^2}$$

(3) continued

$$r_{i,j} = a \cosh \eta_i \sin \xi_j$$

and $P\Delta V$ is the total source strength of the arbitrary control volume. While the subscripts i and j refer to spatial location, the super subscript m refers to time level. All the other terms in the equations are defined in the Nomenclature.

The finite difference representation of the heat conduction equation, expression (2), can now be put in terms of dimensionless nodal enthalpy, ψ , and dimensionless nodal temperature, θ . These two dependent variables are defined as:

$$\psi = \frac{1}{\rho V} \int_V \rho \frac{(H - H_s^*)}{\Delta H_{sl}} dV = \frac{H - H_s^*}{\Delta H_{sl}} \quad (4)$$

$$\theta = \frac{k}{k_s} \frac{C_{ps} (T - T_m)}{\Delta H_{sl}}$$

In general H in equation (4) refers to the specific enthalpy of the discretized space volume and assumes different forms when the node is in the liquid, solid or in the liquid-solid region.

H_s^* is the specific enthalpy of the solid at its melting point and k is thermal conductivity which assumes conductivity of the liquid or the solid. In the formulation presented here the following assumptions are made; the density of the solid and the liquid are equal, the conductivities and heat capacities of the solid and liquid are independent of temperature, but different from each other.

In the solid region the dimensionless nodal enthalpy, ψ , is negative and is equal to the dimensionless nodal temperature, θ :

$$\psi = \theta = \frac{C_{ps}(T - T_M)}{\Delta H_{sl}} < 0 \quad (5)$$

In the superheated liquid region:

$$\begin{aligned} \psi = 1 + \frac{C_{pl}(T - T_M)}{\Delta H_{sl}} &> 1.0 \\ \theta = \frac{k_l}{k_s} \frac{C_{ps}}{C_{pl}} (\psi - 1) \end{aligned} \quad (6)$$

For an element containing the liquid-solid interface is at the melting point of the metal, ψ is defined by:

$$0 \leq \psi \leq 1.0 \text{ and } \theta = 0 \quad (7)$$

The value of ψ is equal to the weight fraction of the element which is in the liquid state, f_l .

The appropriate forms of equation (4) for an element in the liquid or solid phase are substituted into equation (2). After some manipulation and multiplication by different factors the following common equation is obtained for both cases.

$$\begin{aligned} \frac{\cosh^2 \eta_i - \sin^2 \xi_j}{\Delta F_0} \psi_{i,j}^m + (C_1 + C_2 + C_3 + C_4) \theta_{i,j}^m = \\ \frac{\cosh^2 \eta_i - \sin^2 \xi_j}{\Delta F_0} \psi_{i,j}^{m-1} + (C_1 \theta_{i-1,j}^m + C_2 \theta_{i+1,j}^m + C_3 \theta_{i,j-1}^m + \\ C_4 \theta_{i,j+1}^m) + \frac{P \Delta V}{2\pi k_s r_{i,j} \Delta n \Delta \xi} \frac{C_{ps}}{\Delta H_{sl}} \end{aligned} \quad (8)$$

IV. BOUNDARY CONDITIONS AND SOLUTION OF THE FINITE DIFFERENCE EQUATIONS

The initial and boundary conditions are derived based on the following assumptions.

The metal is initially at room temperature, $T = T_0$.

The absorbed heat flux in the circular region of the surface is in general $q = q(r)$ and the problem is solved for the two special cases of constant and Gaussian distribution of the absorbed heat flux.

Equation (8) is then subject to the following boundary conditions:

(i) $t = 0, 0 \leq \eta < \infty, 0 \leq \xi \leq \pi/2,$

$$\psi_{i,j} = \theta_{i,j} = - \frac{C_{ps}(T_M - T_0)}{\Delta H_{sl}} \quad (9)$$

(ii) $t > 0, \eta = 0, 0 \leq \xi \leq \pi/2 \quad C_1 = 0$

(a) $q = Q/\pi a^2 = \text{constant}$

(b) $q = q_0 e^{-2 \sin^2 \xi} \quad (10)$

(iii) $t > 0, \xi = \pi/2, \eta > 0$

$$C_4 = 0 \quad (11)$$

(iv) $t > 0, \eta \rightarrow \infty, 0 \leq \xi \leq \pi/2$

$$\psi_{i,j} = \theta_{i,j} = - \frac{C_{ps}(T_M - T_0)}{\Delta H_{sl}} \quad (12)$$

(v) $t > 0, \eta > 0, \xi = 0$

$$C_3 = 0 \quad (13)$$

Boundary condition (iii) assumes that convective and radiative heat loss from the surface are negligible. This is in line with our earlier calculations (1).

Finally, for the boundary conditions (ii) to (v) the value of $P\Delta V$ in equation (8) is zero except at the circular region on the surface, boundary condition (ii), when it is specified by the following equations:

$$P\Delta V = \pi a^2 \int_{\xi_j - \Delta\xi/2}^{\xi_j + \Delta\xi/2} q(\xi) \sin(2\xi) d\xi \quad (14)$$

For case (a) $q = \text{constant}$

$$P\Delta V = 2\pi a^2 q \sin\xi_j \cos\xi_j \sin\Delta\xi \quad (15)$$

For case (b) $q = q_0 e^{-2\sin^2\xi}$

$$P\Delta V = \frac{\pi a^2 q_0}{2} [e^{-2\sin^2(\xi - \frac{\Delta\xi}{2})} - e^{-2\sin^2(\xi + \frac{\Delta\xi}{2})}] \quad (16)$$

The system of algebraic equations, equation (8) for the different elements in the oblate spheroidal coordinate were solved using the Gauss-Seidel iterative method. The computer logic presented below closely follows that described by Sparrow et. al. (4). However, the family of equations and specific relationships between dimensionless nodal enthalpy and temperature developed here are different in problem geometry, coordinate system, boundary conditions and the fact that superheat in the liquid is taken into consideration.

Once the solution has been obtained for a time level $m - 1$, the calculation for the following time level m is started by initially setting all the $\psi_{i,j}^m$ values as equal to the previous time level. Then using the equations (5) to (7) the left-hand side, L.H.S., of equation (8) is written in terms of dimensionless nodal enthalpy as follows; If $\psi_{i,j}^m < 0$ the element is in the solid,

$\psi_{i,j}^m = \theta_{i,j}^m$, and both the left and right-hand sides of equation (8) are less than zero. On the other hand, if $0 < \psi_{i,j}^m < 1.0$, the element contains the liquid-solid interface and the following relationship holds for the R.H.S. of equation (8).

$$0 < \text{R.H.S.} < \frac{\cosh^2 \eta_i - \sin^2 \xi_j}{\Delta F_0} \quad (17)$$

Finally, if $\psi_{i,j}^m > 1.0$ the element is in the superheated liquid region and substitution of equation (6) into equation (8) yields:

$$\text{R.H.S.} > \frac{\cosh^2 \eta_i - \sin^2 \xi_j}{\Delta F_0} \quad (18)$$

The sign and the magnitude of the right-hand side of equation (8) is used to determine the applicable $\psi_{i,j}$, $\theta_{i,j}$ relationship, equations (5) to (7). For example, if using the most recently computed values of ψ^m at the four points surrounding i, j yields a R.H.S. corresponding to equation (18), this means that $\psi_{i,j}^m > 1.0$ and the new value of $\psi_{i,j}^m$ is obtained from:

$$\psi_{i,j}^m = \frac{\text{R.H.S.} + (C_1 + C_2 + C_3 + C_4) \cdot k_l C_{ps} / k_s C_{pl}}{(\cosh^2 \eta_i - \sin^2 \xi_j) / \Delta F_0 + (C_1 + C_2 + C_3 + C_4) k_l C_{ps} / k_s C_{pl}} \quad (19)$$

The new value of $\psi_{i,j}^m$ is compared with the old guess value to see if it satisfies a convergence criterion, $|\psi_{i,j}^m (\text{new}) - \psi_{i,j}^m (\text{old})| \leq 0.005$.

This process is then repeated throughout the mesh in a definite order a number of times for each time step until the convergence criteria is met, after which the next time step, $\psi_{i,j}^{m+1}$ is calculated using the same procedure.

V. RESULTS AND DISCUSSIONA. Uniform Heat Flux

The analytical solution to the thermal fields in a semi-infinite solid substrate subjected to a uniform heat flux over a circular region on its bounding surface is given by Carslaw and Jaeger (5). The solution may be simplified to give the temperature at the center of the circular region, $T(0,0)$. One form of this expression is:

$$\frac{k_s [T(0,0) - T_0]}{qa} = \frac{2\sqrt{\alpha_s t}}{\sqrt{\pi} a} \left[1 - \sqrt{\pi} \operatorname{ierfc} \frac{a}{2\sqrt{\alpha_s t}} \right] \quad (20)$$

Equation (20) was used to calculate the curve associated with the vertical axis on the right side of Figure 2. This plot shows that for a given radius of the circular region, a , there is a minimum heat flux required if the center of the circular region is to reach a given temperature, e.g. the melting point of the substrate. That is, for small values of $a/2\sqrt{\alpha_s t}$, large Fourier numbers $\alpha_s t/a^2$, the left hand side of equation (20) approaches one - the temperature, $T(0,0)$, approaches its maximum steady state value. For example, in aluminum* the product of absorbed heat flux and the radius of the circular region $qa \geq 1.45 \times 10^5$ W/m if the center of the circular region is to ever reach the melting point.

Similarly one may anticipate that specific qa values could be deduced from numerical computations for the initiation of surface

*Properties of aluminum used in the calculations are listed in Table I.

melting and for any surface temperature at the center of the liquid zone up to the vaporization temperature. Figure 3 shows a plot of the data obtained from approximately 15 computer runs (over two hundred points). Note the similarity between the curve associated with the vertical axis on the right side of this Figure and that in Figure 2. The numerator on the vertical axis includes the sum of $k_l(T-T_M)$, $k_s(T_M-T_0)$ and $k_s \Delta H_{sl}/C_{pl}$. The latter is used here to denote the equivalent temperature change for the melting of the substrate. The curve in Figure 3 approaches $\sim 97\%$ of the steady state value for small $a/2\sqrt{\alpha_s t}$ values which is sufficiently accurate considering other approximations used in the computer heat flow model. For an aluminum substrate, minimum values of $qa \approx 2.3 \times 10^5$ W/m and $qa \approx 4.2 \times 10^5$ W/m are deduced from this curve for the initiation of surface melting and for a surface temperature $T(0,0) = T_v$. For example when $qa = 2.86 \times 10^5$ the calculated maximum steady state temperature at the center of the molten zone is 1607 K.

Equation (20) can also be written in the following form:

$$\frac{\sqrt{\pi} [T(0,0) - T_0] \sqrt{k_s \rho_s C_{ps}}}{2 q \sqrt{t}} = 1 - \sqrt{\pi} \operatorname{erfc} \frac{a}{2\sqrt{\alpha_s t}} \quad (21)$$

The left hand side of equation (21) is now the ratio of the surface temperature of a semi-infinite solid subjected to a uniform heat flux over its entire surface to the temperature $T(0,0)$ at the center of the circular region. Alternatively the L.H.S. of equation (21) can be viewed as the ratio of $q\sqrt{t}|_{1-D}$ in the one-dimensional to the $q\sqrt{t}|_{2-D}$ in the two-dimensional heat flow problems,

respectively. In either case the curve associated with the vertical axis on the left side of Figure 2 shows that for values of $a/2\sqrt{\alpha_s t} \geq 2.0$, $\alpha_s t/a^2 \leq 0.0625$, heat flow is essentially unidirectional. A similar plot obtained from the computer heat flow model during surface melting is shown in Figure 3. The general form of the two curves in Figure 3 permit the deduction of the following information for any absorbed heat flux and radius of the circular region. First, for a given value of q_a and $T(0,0)$ one may establish whether lateral heat flow in the substrate can be ignored. As example, for an aluminum substrate, when $q_a \geq 1.4 \times 10^6 \text{ W/m}$ heat flow is essentially in one dimension for $T(0,0)$ temperatures up to T_v . Second, the time for the center of the circular region to reach any temperature above the melting point of the substrate can be deduced. For example, for an absorbed uniform heat flux of 10^9 W/m^2 and a spot radius $a = 380\mu\text{m}$, $T(0,0)$ will reach 1700K in $2.1 \times 10^{-3} \text{ sec}$. Furthermore, the maximum temperature achieved at the center of the circular region would be 2238K.

Figure 4 shows the general relationship developed from numerical computations between temperature at the center of the circular region and the product of absorbed heat flux and melt depth, qz , for an aluminum substrate. z in this figure denotes melt depth along the z -axis at the center of the circular region $r = 0$. For any value of q and a , for which the product $qa \geq 2.3 \times 10^5 \text{ W/m}$, time for $T(0,0)$ to reach a given temperature can be deduced from Figure 3. The corresponding melt depth along the z -axis can then be found from Figure 4. For example, for uniform heat fluxes of $3 \times 10^8 \text{ W/m}^2$ and 10^9 W/m^2 absorbed over circular regions with

radii of $\approx 1587\mu\text{m}$ and $\approx 476\mu\text{m}$, respectively ($qa \approx 4.76 \times 10^5 \text{ W/m}$) the corresponding times and melt depths during melting of an aluminum substrate when $T(0,0) = T_v$ are $t = 5.4 \times 10^{-2} \text{ sec}$ and $t = 4.86 \times 10^{-3} \text{ sec}$ from Figure 3 and $z = 933\mu\text{m}$ and $z = 280\mu\text{m}$ from Figure 4, respectively. Similar information can also be obtained from these two figures for any $T(0,0)$ temperature between T_M and T_v . While the data plotted in Figure 3 can be used for any substrate material, the curve in Figure 4 is specifically calculated for an aluminum substrate. Similar curves can readily be generated for other substrate materials using the equations and computations procedure outlined in the previous sections. As noted above, for values of $qa \geq 1.4 \times 10^6 \text{ W/m}$ heat flow in the aluminum substrate is essentially one-dimensional and the corresponding times and melt depths from Figures 3 and 4 would be identical to those previously described (1) when the physical and thermal properties of the substrate are the same.

An important finding from this work is that for a given value of $T(0,0)$ at the center of the circular region the dimensionless temperature distribution in the substrate material during melting and solidification is identical for any combination q and a as long as $qa = \text{constant}$. Figure 5 shows the shape and location of several isotherms, including the liquid-solid interface, in an aluminum substrate material subjected to a uniform heat flux q over a circular region of radius a where the product $qa = 4.76 \times 10^5 \text{ W/m}$. Note that these are the isotherms at the instant $T(0,0)$ reaches the vaporization temperature of aluminum $T_v = 2723\text{K}$ and the axis used are made dimensionless dividing them by the radius of

the circular region. Identical dimensionless plots were obtained from several computer runs where q and a values were varied over large ranges while the product qa was kept constant.

Figure 6 shows the dimensionless plots of the location and shape of the liquid-solid interface for $qa = 4.76 \times 10^5$ W/m during melting and subsequent solidification of an aluminum substrate. In these simulations the heat flux was removed, $P\Delta V$ in equation (15) was set equal to zero, as soon as $T(0,0)$ reached the vaporization temperature. As in the previous one-dimensional heat flow model (1) melting of the substrate continues until heat flux in the liquid and the solid at the liquid-solid interface become equal - the interface velocity approaches zero. Decreasing values of $a/2\sqrt{\alpha_s t}$, increasing time, denote the successive positions of the liquid-solid interface during the melting and the subsequent solidification sequence. The curve in Figure 6 identified by $a/2\sqrt{\alpha_s t_{\max}}$ shows the shape and position of the liquid-solid interface when the melt along the z-axis reaches its maximum depth. It is interesting to note that due to the lower temperature gradients in the liquid near the periphery of the molten region solidification in this region commenced while melting in the central region was still continuing. The higher lateral heat loss thus results in liquid-solid interface shapes closer to that of a spherical geometry during the solidification sequence. Finally, both dimensionless time, $a/2\sqrt{\alpha_s t}$, and liquid-solid interface shapes and velocities remained the same in these types of dimensionless plots as long as the product qa was kept constant.

Figures 7 and 8 show the effect of increasing the product qa on the geometry and the location of the liquid-solid interface at the

instant the temperature $T(0,0)$ reaches 2100K and 2723K, respectively. The curves for $qa \approx 1.9 \times 10^6 \text{ W/m}$ are in the range where heat flow can be assumed to be essentially one-dimensional and the shape of the isotherms verify this fact. On the other hand, with decreasing values of qa , lateral heat flow becomes significant and the liquid-solid interfaces assume shapes closer to the oblate spheroidal coordinate illustrated in Figure 1.

Liquid-solid interface velocities during melting and subsequent solidification of an aluminum substrate along the z-axis and the r-axis as a function of qa are shown in Figures 9 and 10. These data show that for a given value of qa the interface velocity, R , is directly proportional to the absorbed heat flux during both melting and subsequent solidification. Furthermore, for any given value of qa interface velocities along the r-axis, on the specimen surface, are higher than those along the z-axis.

Figures 9 and 10 also show that in the one-dimensional heat flow range, $qa \geq 1.4 \times 10^6 \text{ W/m}$, liquid-solid interface velocities are essentially identical to that previously reported (1). Interface velocities rapidly increase to a maximum value* once surface melting commences and drop off to zero sometime after $T(0,0) = T_v$ and the heat flux is removed. During subsequent solidification interface velocities increase with distance solidified but always remain lower than that during melting. For example, for an absorbed heat flux of $q = 10^9 \text{ W/m}^2$ and $qa = 1.905 \times 10^6 \text{ W/m}$ ($a = 1905 \mu\text{m}$)

*the rapid increase after the initiation of melting occurs over very small fractional distances and is not shown in these Figures.

the calculated interface velocities along the z-axis midway during the melting and the solidification sequences ($z/z_{\max} = 0.5$) are ~ 0.17 m/sec and ~ 0.15 m/sec, respectively. The corresponding interface velocities in the radial direction, on the specimen surface, at $r/r_{\max} = 0.5$ are ~ 3 m/sec and ~ 0.32 m/sec, respectively. Increasing the absorbed heat flux by a factor of five while the product qa is kept constant ($a = 381 \mu\text{m}$) would result in a corresponding factor of five increase in the interface velocities calculated above.

For values of $2.3 \times 10^5 < qa < 1.4 \times 10^6 \text{ W/m}$ the liquid-solid interface velocities along the z-direction are always lower during melting than during solidification. This is simply from the increasing lateral heat loss due to the increased divergency of heat flow with decreasing values of qa in this range. However, for lower values of qa , e.g. $qa = 4.76 \times 10^5 \text{ W/m}$, interface velocities along the r-axis are approximately the same during melting and solidification. For example, at an absorbed heat flux of $q = 10^9 \text{ W/m}^2$ and $qa = 4.76 \times 10^5 \text{ W/m}$ ($a = 476 \mu\text{m}$) the calculated interface velocities along the z-axis midway during the melting and the solidification sequences are ~ 0.063 m/s and ~ 0.24 m/s, respectively. The corresponding values in the radial direction, from Figure 10, are ~ 0.68 m/s and ~ 0.57 m/s, respectively.

No attempt is made here to quantitatively describe the more complex relationships between absorbed heat flux and the ratio of temperature gradient in the liquid at the liquid-solid interface and growth velocity, G_L/R . However, qualitative relationships are easily deduced from Figures 4 to 10. In general, for a given value of qa temperature gradient at the liquid-solid interface increases

proportionally with increasing values of absorbed heat flux, q .

On the other hand, since interface velocities also increase with increasing values of q , the ratio G_L/R is not affected. The maximum values of G_L/R during solidification are noted at the initial stages of solidification, when R is almost zero and the temperature gradient in the liquid is high. Furthermore, superheat in the liquid is rapidly consumed while interface velocities increase with increasing distance solidified - resulting in a rapid decrease in G_L/R . Figures 6, 9 and 10 also show that temperature gradients in the liquid are higher and interface velocities are lower along the z -axis during solidification, therefore, the ratio G_L/R assumes its maximum value along this axis.

B. Gaussian Absorbed Heat Flux

In order to systematically analyze the effect of Gaussian absorbed heat flux distributions on the surface melting and solidification parameters and relate same to the previous case of uniform absorbed heat flux, the relationship between the two heat flux distributions shown in Figure 11 was first developed. Inside the circular region the oblate spheroidal coordinate $\eta = 0$, Figure 1. Equation (16) for case (b) can thus be written in its equivalent form in cylindrical coordinates:

$$q_G = q_0 e^{-2r^2/a^2} \quad (22)$$

If we assume that the total power absorbed, Q , in the circular region is identical for the uniform and Gaussian heat flux distributions, as shown in Figure 11, then the following relationship is deduced:

$$q_{\text{uniform}} = \frac{q_0}{2.313} \quad (23)$$

where q_0 is the absorbed heat flux at the center of the circular region and will be referred to hereafter as the maximum absorbed heat flux.

The equations and solution methods described in previous sections were used to generate data for the rapid melting and subsequent solidification of an aluminum substrate material. The relationship between melt depth along the z-axis, maximum absorbed heat flux, q_0 , and temperature at the center of the circular region is shown in Figure 4. The data indicate that for a given temperature $T(0,0)$ and total power absorbed, Q , melt depths in the Gaussian heat flux distribution are ~ 2.313 times shallower than that obtained in the case of the uniform absorbed heat flux.

Computer calculations also showed that dimensionless temperature distributions during surface melting and subsequent solidification are identical if the product $q_0 a$ is kept constant while q_0 and a are varied. Figure 12 shows the shape and location of several isotherms, including the liquid-solid interface ($T = 933\text{K}$), during surface melting of an aluminum substrate subjected to a Gaussian absorbed heat flux distribution. These are the isotherm shapes at the instant when $T(0,0) = 2723\text{K}$.

Figure 13 shows the effect of increasing the product $q_0 a / 2.313$ on the geometry and the location of the liquid-solid interface at the instant when $T(0,0)$ reaches the vaporization temperature of the aluminum substrate. Increasing the product $q_0 a$ results in shallower melt depths as anticipated. It should be noted that the

center of the circular region reaches the vaporization temperature of the substrate for $q_0 a / 2.313$ values lower than the criteria developed for the uniform absorbed heat flux, $qa \geq 4.2 \times 10^5 \text{ W/m}$. This is simply due to the higher absorbed heat flux at the center of the circular region in the Gaussian distribution.

Figures 14 and 15 compare the shapes and locations of the liquid-solid interfaces between uniform and Gaussian heat flux distributions when $T(0,0)$ reaches 1420K and 2723K, respectively. As indicated above, for a given total absorbed heat flux equation (23) holds and the center of the circular region heats up much more rapidly when the heat flux has a Gaussian distribution. The melt-depth along the z-axis is shallower, while the melt width is smaller due to the diminishing absorbed heat flux with increasing r in the circular region.

Figure 16 shows dimensionless plots of the location and shape of the liquid-solid interface for $q_0 a / 2.313 = 4.76 \times 10^5 \text{ W/m}$ during melting and subsequent solidification of the surface of an aluminum substrate. As before, the heat flux was removed as soon as $T(0,0)$ reached the vaporization temperature. Note the similarity between Figure 16 and 6, the total absorbed power over the circular region was the same in the two cases. The higher maximum heat flux in the Gaussian distribution results in higher temperature gradients, shallower melt depths and shorter times - larger values of $a / 2\sqrt{\alpha_s t}$. For example, for a total absorbed heat flux $Q \approx 0.71 \text{ KW}$ over a circular region of radius $a \approx 476 \mu\text{m}$ the times for the interface to reach its maximum melt depth for uniform and Gaussian heat flux distributions are 5.9×10^{-3} second 6.25×10^{-4} sec, respectively.

Liquid-solid interface velocities during melting and subsequent solidification of an aluminum substrate along the z-axis and the r-axis as a function of $q_0 a / 2.313$ are shown in Figures 17 and 18, respectively. Note that in these two figures the interface velocity, R , is divided by $q_0 / 2.313$ - the equivalent heat flux in the uniform distribution. These data again show that for a given value of $q_0 a / 2.313$ the interface velocity is directly proportional to the absorbed heat flux, and that velocities along the r-axis are higher than those along the z-axis. Furthermore, as the product of $q_0 a / 2.313$ decreases, heat flow lines, during solidification, become more divergent resulting in a corresponding relative increase in interface velocities along the z-axis. Finally, for a given total power absorbed, the calculated interface velocities along the z-axis in the Gaussian distribution are higher than those for the uniform absorbed heat flux. For example, at an absorbed heat flux of $q_0 / 2.313 = 10^9 \text{ W/m}^2$ and $q_0 a / 2.313 = 4.76 \times 10^5 \text{ W/m}$ ($a = 476 \mu\text{m}$) the interface velocities from Figure 17 during melting and solidification are 0.27 m/s and 0.47 m/s, respectively. The corresponding values for the same total power absorbed uniformly over the circular region were previously noted to be $\sim 0.063 \text{ m/s}$ and $\sim 0.24 \text{ m/s}$, respectively. The same observation holds true when interface velocities in the radial direction are compared, Figures 18 and 10.

VI. SUMMARY

The concepts of an enthalpy model recently proposed are used to develop the heat flow equations in oblate spheroidal coordinates for melting and solidification of the surface of a semi-infinite solid subjected to a variable heat flux in a circular region on its bounding surface. While numerical solutions are presented for step function uniform and Gaussian heat flux distributions, the equations and numerical technique developed can be applied to heat fluxes that are both a function of position and time. General trends established relate the important melting and solidification parameters to absorbed heat flux, radius of the circular region and time using the thermophysical properties of an aluminum substrate material. No account is taken of the changes in reflectivity of substrate with temperature or convection in the molten region. The former can be readily included in the generalized equations when experimentally measured values become available, while the latter could be approximately accounted for by increasing the thermal conductivity of the liquid.

NOMENCLATURE

a	radius of the circular region, m
C	integration constant
C_p	specific heat, $\text{J Kg}^{-1} \text{K}^{-1}$
f_l	fraction liquid
Fo	Fourier number ($k_s t / \rho C_p a^2$); ΔF_o dimensionless time step.
H	specific enthalpy, J Kg^{-1}
ΔH_{sl}	heat of fusion, J Kg^{-1}
k	thermal conductivity, $\text{J m}^{-1} \text{s}^{-1} \text{K}^{-1}$
P	rate of heat generation per unit volume, W m^{-3}
q	absorbed heat flux, W m^{-2}
Q	rate of total absorbed heat, W
r	radial coordinate, m
t	time, s
t_m	time for the surface of a material to reach its melting temperature,
t_{max}	time for a material to achieve a maximum melt depth,
t_v	time for surface of a material to reach its vapor- ization temperature,
T_o	ambient temperature K
T_M	melting temperature K
T_s	surface temperature K
T_v	vaporization temperature K
V	volume, m^3
ΔV	volume of discretized domain
z	axial coordinate, m
α	thermal diffusivity ($K / \rho C_p$), $\text{m}^2 \text{ s}^{-1}$

η oblate spheroidal coordinate
 θ dimensionless temperature variable, equation (4)
 ξ oblate spheroidal coordinate
 ψ dimensionless enthalpy variable, equation (4)
 ρ density Kg m^{-3}

Subscripts

i, j nodal point subscripts in η and ξ directions,
respectively
 l liquid region
 s solid region

Superscripts

m time level

ACKNOWLEDGEMENT

This research was sponsored by the Defense Advanced Research Projects Agency and was monitored by the Office of Naval Research under Contract Number N00014-78-C-0275. Technical monitor of the contract was Dr. B. A. MacDonald.

REFERENCES

1. S. C. Hsu, S. Chakravorty, R. Mehrabian, Met. Trans. B., 1978, Vol. 9B, p. 221.
2. G. E. Schneider, A. B. Strong and M. M. Yovanovich, "Finite Difference Modelling of the Heat Conduction Equation in General Orthogonal Curvilinear Coordinates Using Taylor Series Expansion", Proceedings of AICA, International Symposium on Computer Methods for Partial Differential Equations, edited by R. Vichnevetsky, pp. 312-317 AICA, New Brunswick, N.J. (1975).
3. G. E. Schneider, A. B. Strong and M. M. Yovanovich, AIAA paper 75-707, AIAA 10th Thermophysics Conference in Denver, Colorado, May, 1975.
4. N. Shamsundar and E. M. Sparrow, Journal of Heat Transfer, 1975, p. 333.
5. H. S. Carslaw and J. C. Jaeger, Conduction of Heat in Solids, Oxford University Press, Second Edition, 1973.

LIST OF FIGURE CAPTIONS

Figure 1. Two-dimensional spheroidal coordinate system and problem geometry for the rapid melting and solidification of a surface layer.

Figure 2. Temperature at the center of a circular region of a semi-infinite solid substrate as a function of applied uniform absorbed heat flux, radius of the circular region and time. The vertical axis on the left gives the ratio between temperatures in one and two-dimensional heat flow.

Figure 3. Temperature at the center of the liquid zone of a semi-infinite solid substrate during surface melting as a function of uniform absorbed heat flux, radius of the circular region and time. The vertical axis on the left gives the ratio of square root of times in one and two-dimensional heat flow.

Figure 4. Temperature at the center of the circular region $T(0,0)$ over which a heat flux is absorbed in an aluminum substrate versus the product of the absorbed heat flux and melt depth in the axial direction away from the surface. q_0 denotes the maximum heat flux at the center of the Gaussian heat flux distribution. See Figure 11 and equation (23).

Figure 5. Shape and location of several isotherms, including the liquid-solid interface ($T = 933K$), during melting of an aluminum substrate subjected to a uniform absorbed heat flux q over a circular region of radius a . The isotherms are drawn at the instant when $T(0,0)=T_v=2723K$.

Figure 6. Liquid-solid interfaces during melting and subsequent solidification of an aluminum substrate subjected to a uniform absorbed heat flux q over a circular region of radius a . The curve marked $T(0,0)=T_v$ shows the location of the interface at which time the heat flux was removed. Decreasing values of $a/2\sqrt{\alpha_s t}$ denote the successive positions of the liquid-solid interface during the melting and the subsequent solidification sequence.

Figure 7. Liquid-solid interfaces during melting of an aluminum substrate subjected to a uniform heat flux q over a circular region of radius a . The interfaces for each constant qa are shown at the instant the center of the circular region reaches the temperature $T(0,0)=2100K$.

Figure 8. Liquid-solid interfaces during melting of an aluminum substrate subjected to a uniform heat flux q over a circular region of radius a . The interfaces for each constant qa are shown at the instant the center of the circular region reaches the vaporization temperature.

Figure 9. The ratio of liquid-solid interface velocity to absorbed heat flux, R/q , as a function of fractional distance, z/z_{\max} , during melting and solidification of an aluminum substrate subjected to a uniform absorbed heat flux, q over a circular region of radius a .

Figure 10. The ratio of liquid-solid interface velocity to absorbed heat flux, R/q , as a function of fractional distance, r/r_{\max} , during melting and solidification of an aluminum substrate subjected to a uniform absorbed heat flux, q over a circular region of radius a .

Figure 11. Relationship between uniform and Gaussian absorbed heat fluxes when the total power absorbed over the circular region is identical.

Figure 12. Shape and location of several isotherms, including the liquid-solid interface ($T=933K$) during melting of an aluminum substrate subjected to a Gaussian absorbed heat flux distribution over a circular region of radius a . The isotherms are drawn at the instant when $T(0,0)=T_v=2723K$.

Figure 13. Liquid-solid interfaces during melting of an aluminum substrate subjected to a Gaussian absorbed heat flux distribution over a circular region of radius a . The interfaces for each constant $q_0 a/2.313$ are shown at the instant the center of the circular region reaches the vaporization temperature.

Figure 14. Comparison between the shapes and locations of the liquid-solid interfaces during melting of an aluminum substrate subjected to uniform and Gaussian absorbed heat flux distributions at the instant $T(0,0)=1420K$.

Figure 15. Comparison between the shapes and locations of the liquid-solid interfaces during melting of an aluminum substrate subjected to uniform and Gaussian absorbed heat flux distributions at the instant $T(0,0)=T_v$.

Figure 16. Liquid-solid interfaces during melting and subsequent solidification of an aluminum substrate subjected to a Gaussian absorbed heat flux distribution over a circular region of radius a .

Figure 17. The ratio of liquid-solid interface velocity to absorbed heat flux as a function of fractional distance, z/z_{\max} , during melting and solidification of an aluminum substrate subjected to a Gaussian absorbed heat flux distribution over a circular region of radius a.

Figure 18. The ratio of liquid-solid interface velocity to absorbed heat flux as a function of fractional distance, r/r_{\max} , during melting and solidification of an aluminum substrate subjected to a Gaussian absorbed heat flux over a circular region of radius a.

TABLE I

SUMMARY OF PROPERTIES AND SOME CALCULATED
CONSTANTS FOR THE ALUMINUM SUBSTRATE

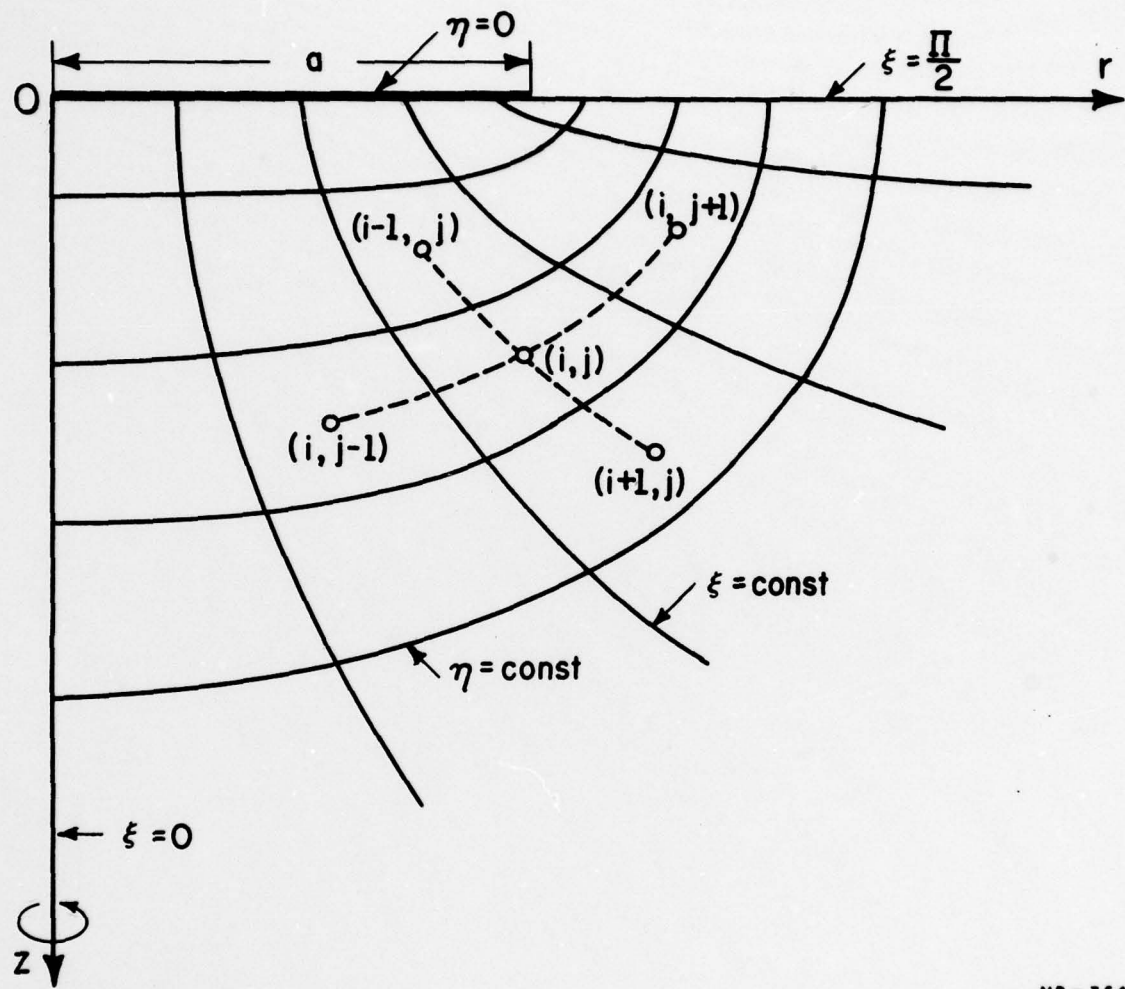
C_{ps}^* = 1048	$J \text{ Kg}^{-1} \text{ K}^{-1}$, Specific Heat of Solid
C_{pl}^* = 1086	$J \text{ Kg}^{-1} \text{ K}^{-1}$, Specific Heat of Liquid
ΔH_{sl} = 3.95×10^5	$J \text{ Kg}^{-1}$, Latent Heat of Fusion
k_s^* = 228	$\text{Wm}^{-1} \text{ K}^{-1}$, Thermal Conductivity of Solid
k_l^{**} = 108	$\text{Wm}^{-1} \text{ K}^{-1}$, Thermal Conductivity of Liquid
T_M = 933	K, Melting Temperature
T_v = 2723	K, Vaporization Temperature
α_s^* = $8.55 \times 10^{-5} \text{ m}^2 \text{ sec}^{-1}$	Thermal Diffusivity of Solid
α_l^{**} = $3.91 \times 10^{-5} \text{ m}^2 \text{ sec}^{-1}$	Thermal Diffusivity of Liquid
$\rho = \rho_s^{***} = \rho_l^{***} = 2545 \text{ Kg m}^{-3}$	Density
$q\sqrt{t}_m _{1-D}$ = $1.5 \times 10^7 \text{ J m}^{-2} \text{ sec}^{-1/2}$	
$q\sqrt{t}_v _{1-D}$ = $4.5 \times 10^7 \text{ J m}^{-2} \text{ sec}^{-1/2}$	
$q\sqrt{t}_{max} _{1-D}$ = $5.5 \times 10^7 \text{ J m}^{-2} \text{ sec}^{-1/2}$	

* Averaged from 298K to Melting Point

** Averaged from Melting Point to Vaporization Temperature

*** Average of Liquid and Solid

1-D Refers to One-Dimensional Heat Flow



MP - 764

Figure 1. Two-dimensional spheroidal coordinate system and problem geometry for the rapid melting and solidification of a surface layer.

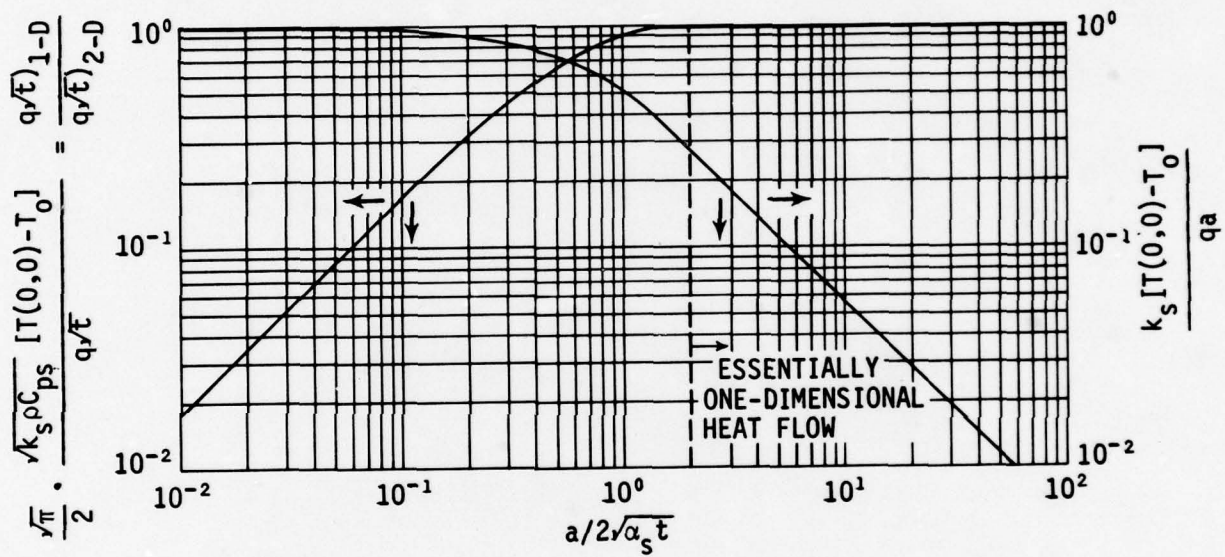


Figure 2. Temperature at the center of a circular region of a semi-infinite solid substrate as a function of applied uniform absorbed heat flux, radius of the circular region and time. The vertical axis on the left gives the ratio between temperature in one and two-dimensional heat flow.

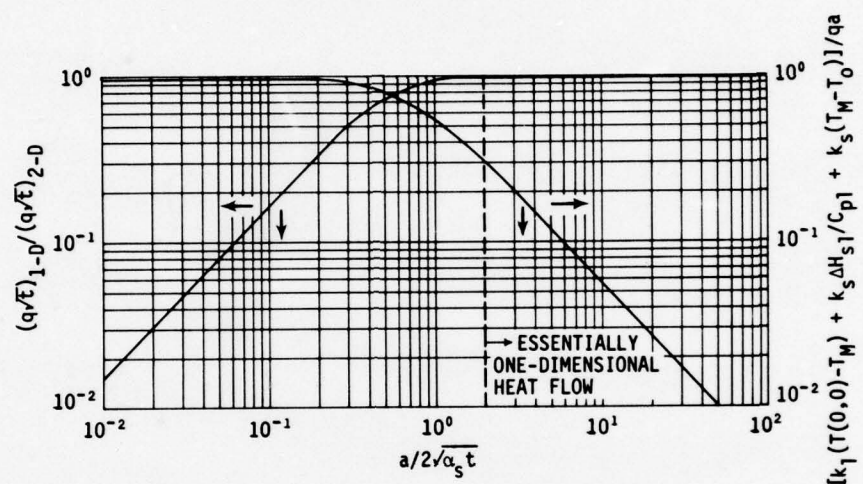


Figure 3. Temperature at the center of the liquid zone of a semi-infinite solid substrate during surface melting as a function of uniform absorbed heat flux, radius of the circular region and time. The vertical axis on the left gives the ratio of square root of times in one and two-dimensional heat flow.

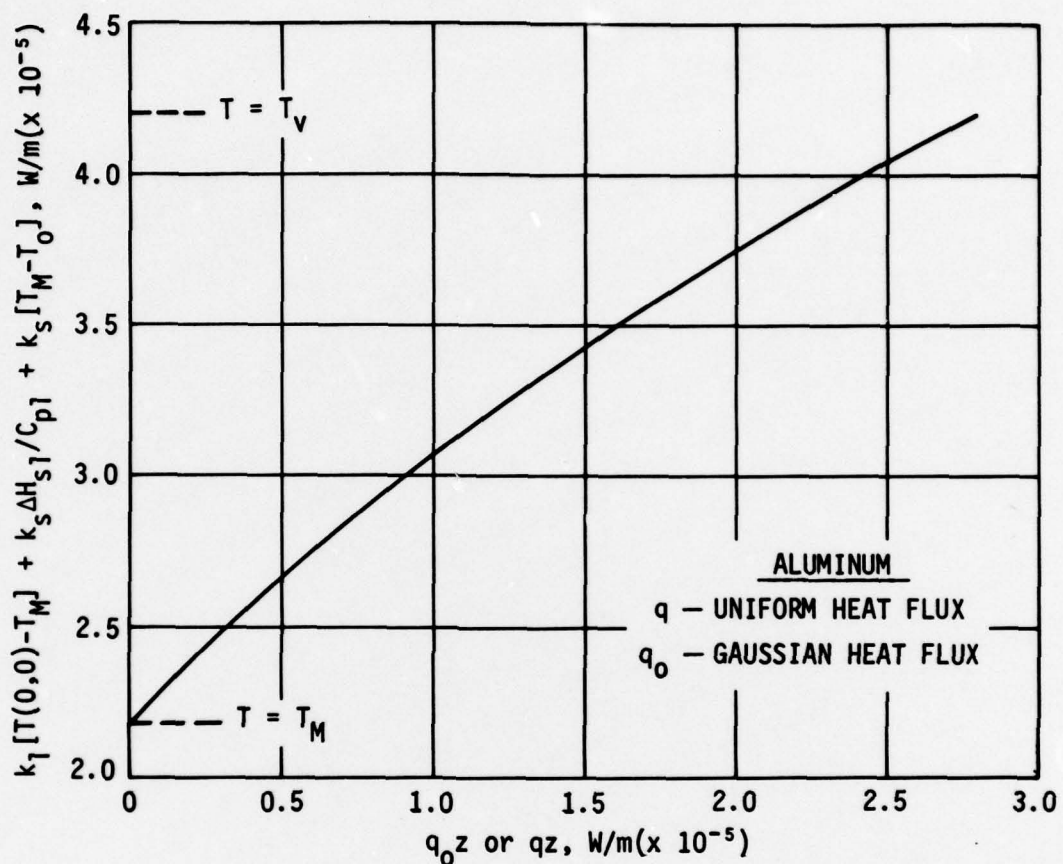


Figure 4. Temperature at the center of the circular region $T(0,0)$ over which a heat flux is absorbed in an aluminum substrate versus the product of the absorbed heat flux and melt depth in the axial direction away from the surface. q_0 denotes the maximum heat flux at the center of the Gaussian heat flux distribution. See Figure 11 and equation (23).

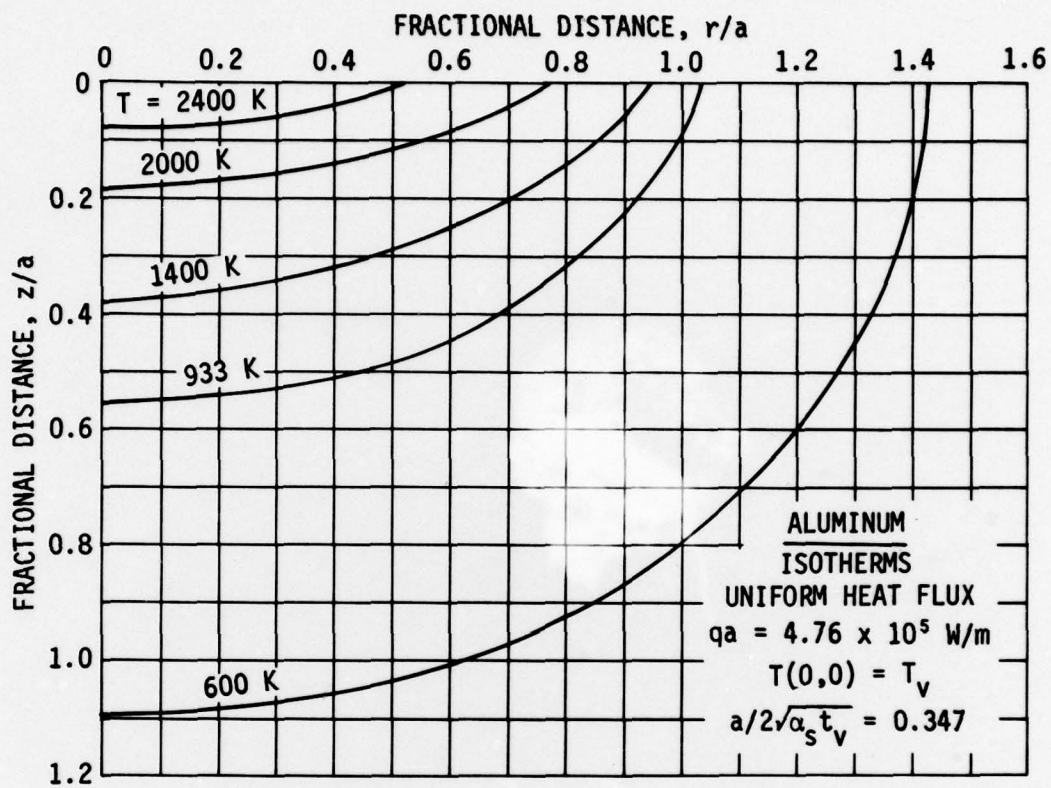


Figure 5. Shape and location of several isotherms, including the liquid-solid interface ($T = 933\text{K}$), during melting of an aluminum substrate subjected to a uniform absorbed heat flux q over a circular region of radius a . The isotherms are drawn at the instant when $T(0,0) = T_v = 2723\text{K}$.

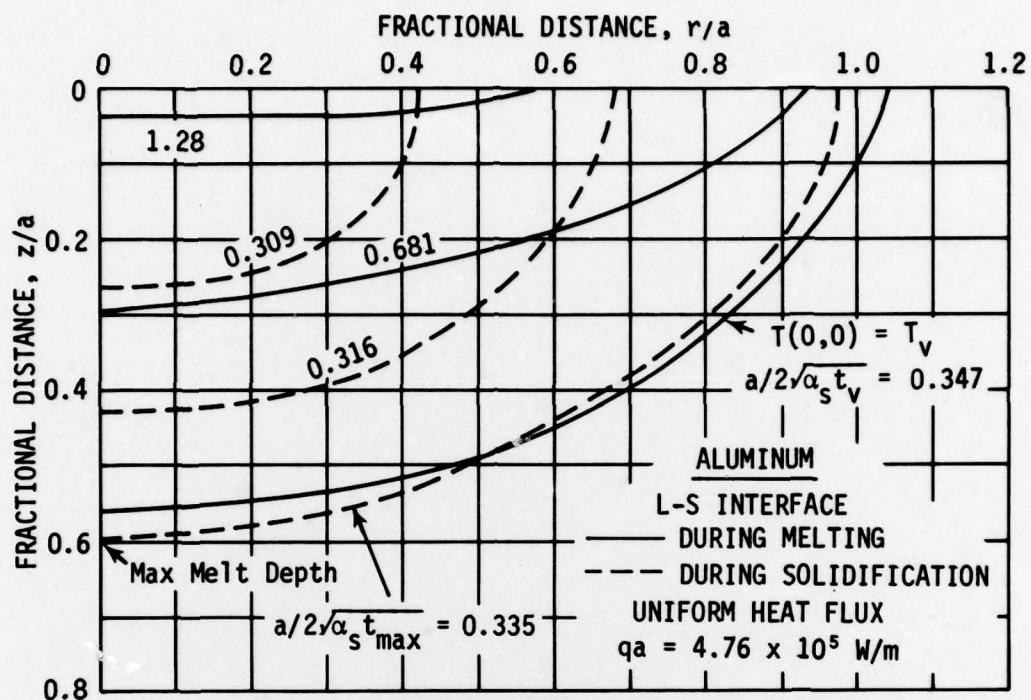


Figure 6. Liquid-solid interfaces during melting and subsequent solidification of an aluminum substrate subjected to a uniform absorbed heat flux q over a circular region of radius a . The curve marked $T(0,0)=T_v$ shows the location of the interface at which time the heat flux was removed. Decreasing values of $a/2\sqrt{\alpha_s} t$ denote the successive positions of the liquid-solid interface during the melting and the subsequent solidification sequence.

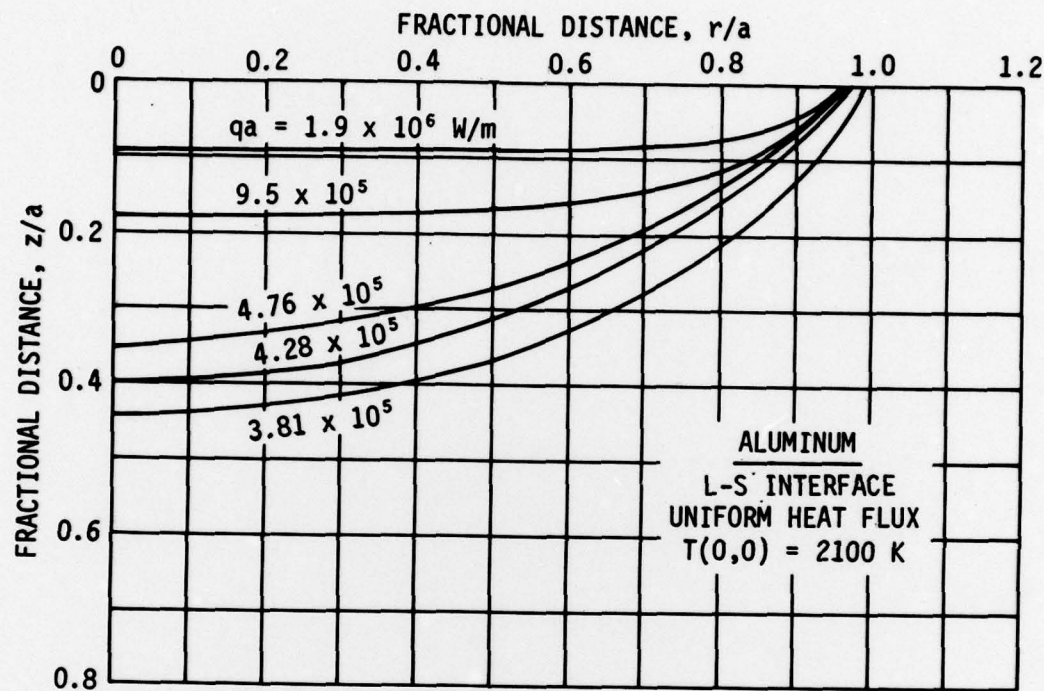


Figure 7. Liquid-solid interfaces during melting of an aluminum substrate subjected to a uniform heat flux q over a circular region of radius a . The interfaces for each constant q_a are shown at the instant the center of the circular region reaches the temperature $T(0,0)=2100\text{K}$.

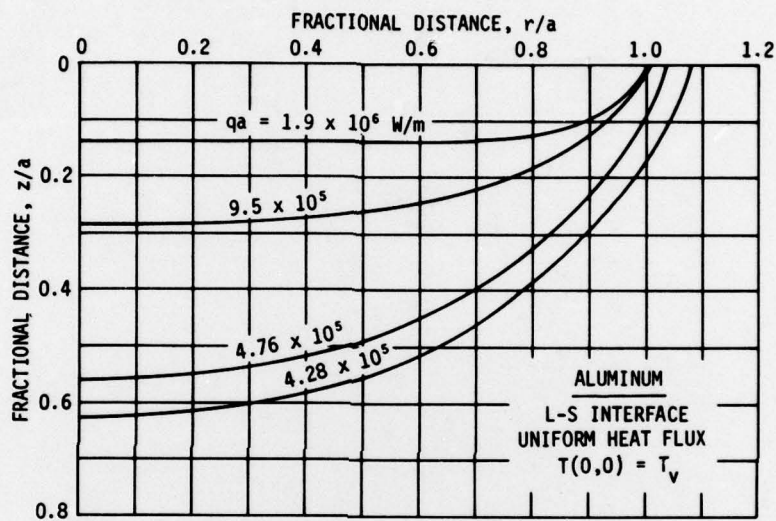


Figure 8. Liquid-solid interfaces during melting of an aluminum substrate subjected to a uniform heat flux q over a circular region of radius a . The interfaces for each constant qa are shown at the instant the center of the circular region reaches the vaporization temperature.

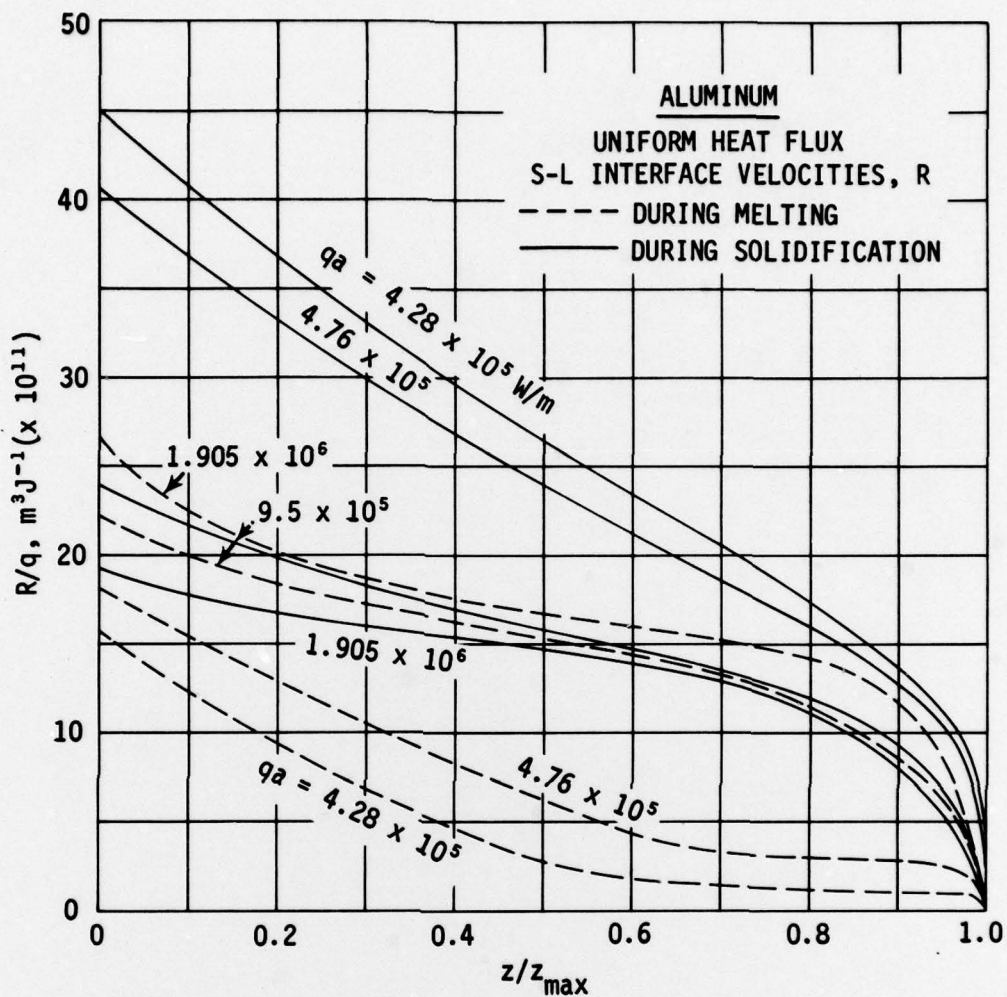


Figure 9. The ratio of liquid-solid interface velocity to absorbed heat flux, R/q , as a function of fractional distance, z/z_{\max} , during melting and solidification of an aluminum substrate subjected to a uniform absorbed heat flux, q over a circular region of radius a .

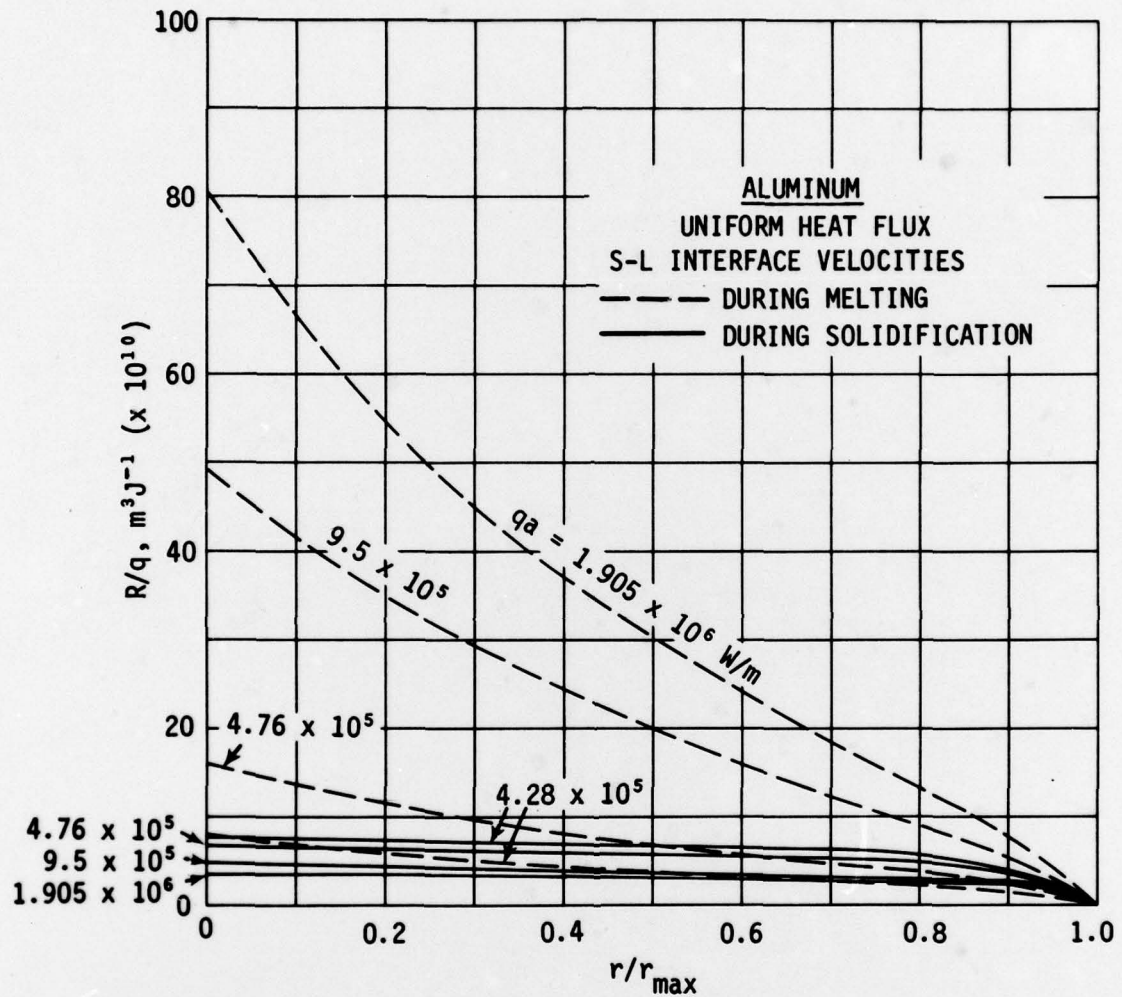


Figure 10. The ratio of liquid-solid interface velocity to absorbed heat flux, R/q , as a function of fractional distance, r/r_{max} , during melting and solidification of an aluminum substrate subjected to a uniform absorbed heat flux, q over a circular region of radius a .

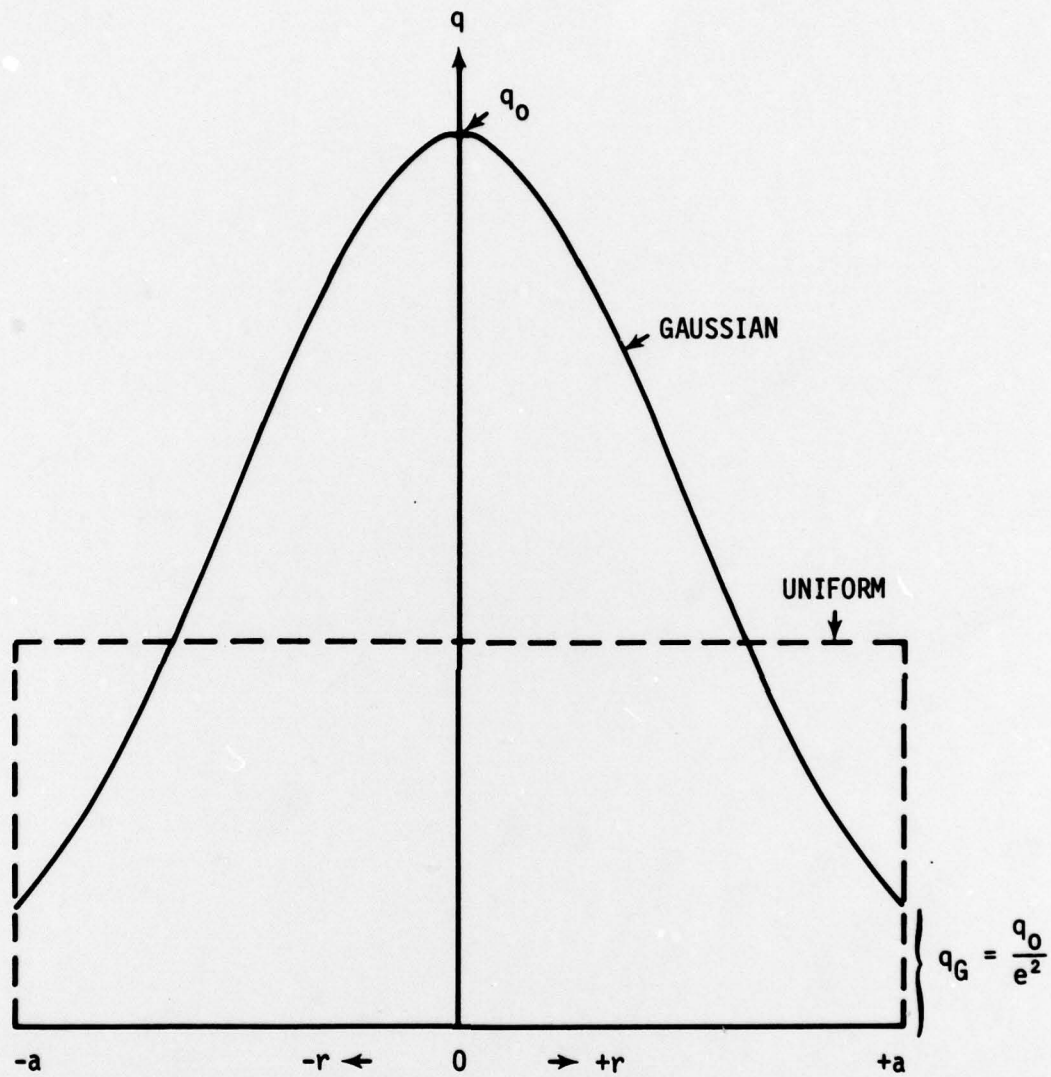


Figure 11. Relationship between uniform and Gaussian absorbed heat fluxes when the total power absorbed over the circular region is identical.

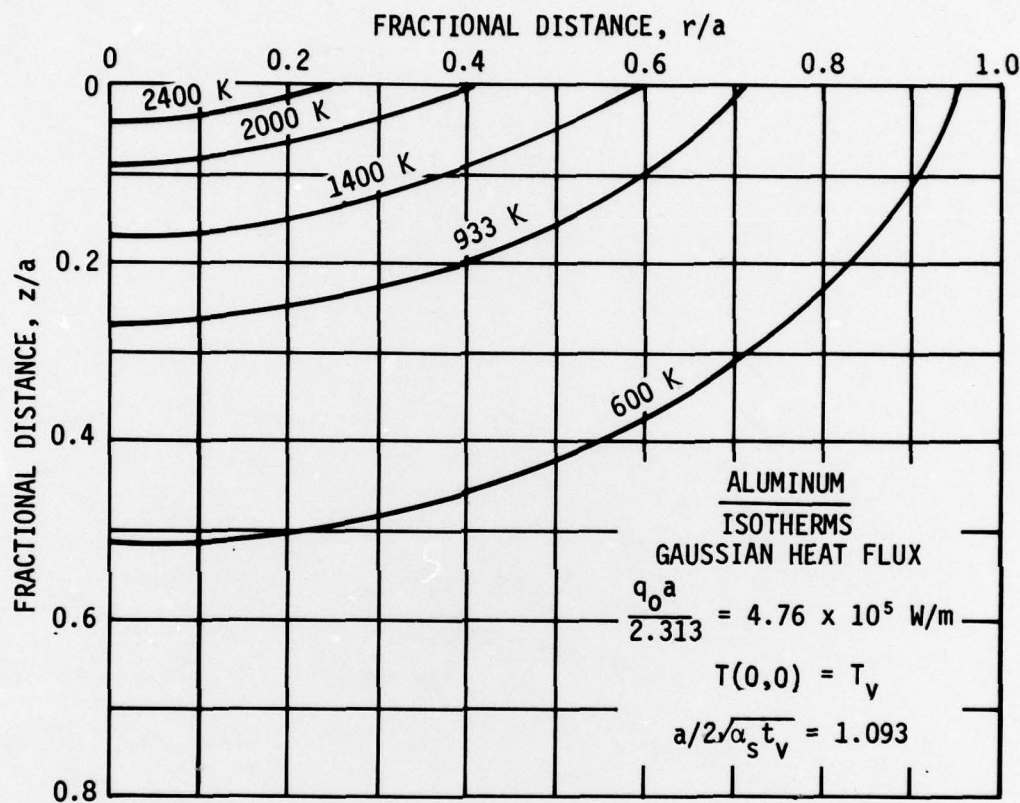


Figure 12. Shape and location of several isotherms, including the liquid-solid interface ($T=933\text{K}$) during melting of an aluminum substrate subjected to a Gaussian absorbed heat flux distribution over a circular region of radius a . The isotherms are drawn at the instant when $T(0,0)=T_v=2723\text{K}$.

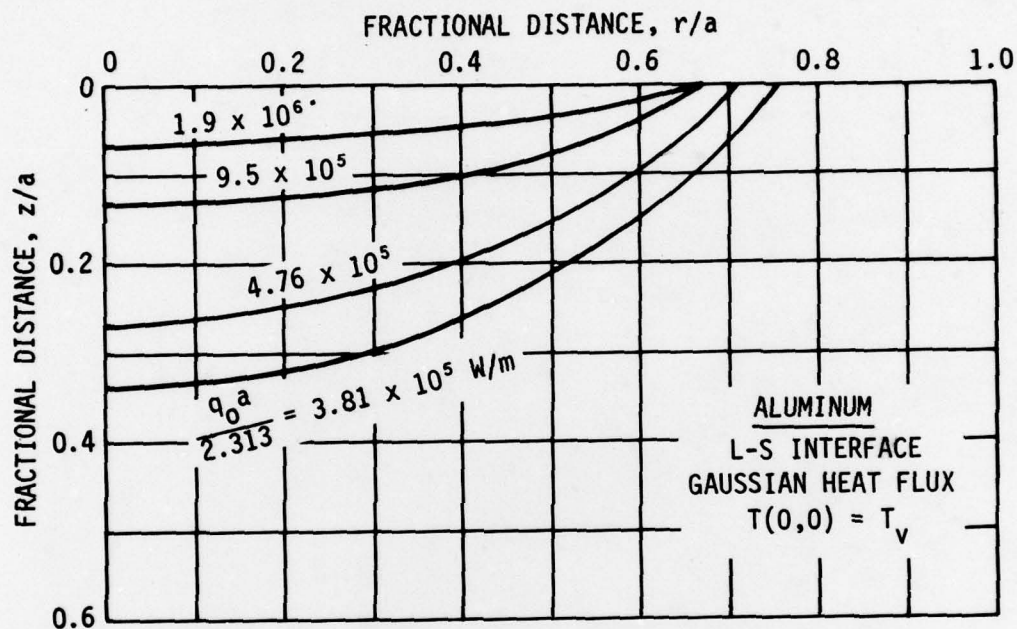


Figure 13. Liquid-solid interfaces during melting of an aluminum substrate subjected to a Gaussian absorbed heat flux distribution over a circular region of radius a . The interfaces for each constant $q_0 a / 2.313$ are shown at the instant the center of the circular region reaches vaporization temperature.

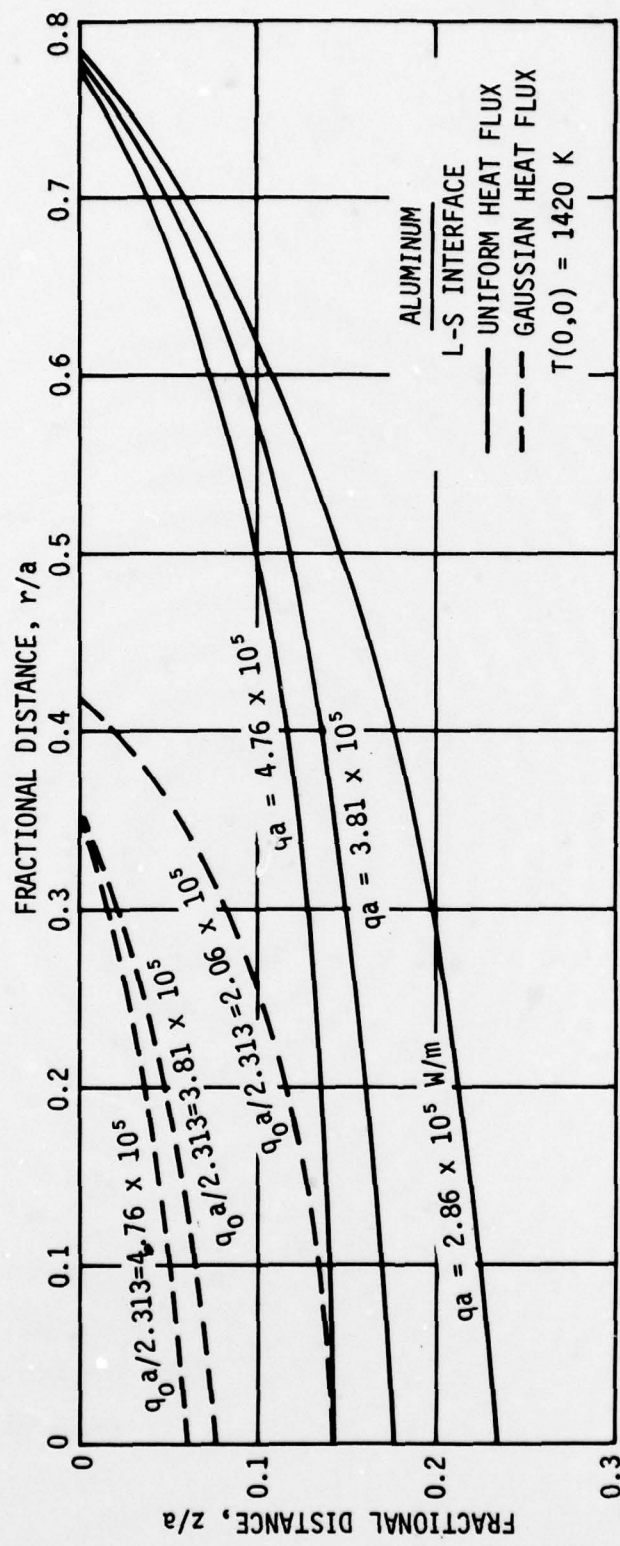


Figure 14. Comparison between the shapes and location of the liquid-solid interfaces during melting of an aluminum substrate subjected to uniform and Gaussian absorbed heat flux distributions at the instant $T(0,0) = 1420\text{ K}$.

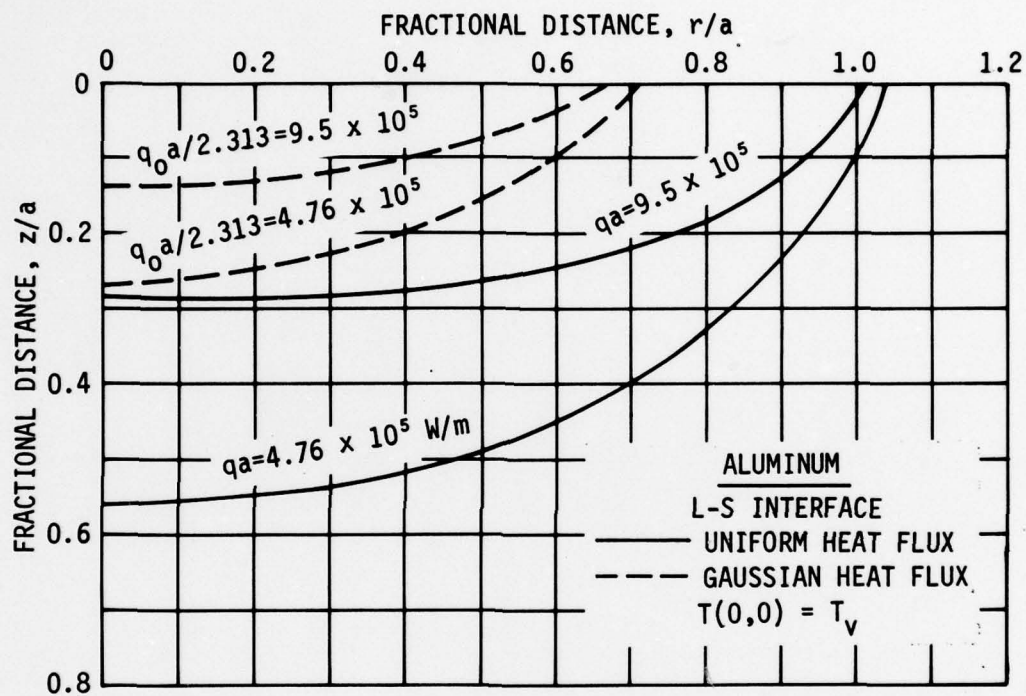


Figure 15. Comparison between the shapes and locations of the liquid-solid interfaces during melting of an aluminum substrate subjected to uniform and Gaussian absorbed heat flux distributions at the instant $T(0,0)=T_v$.

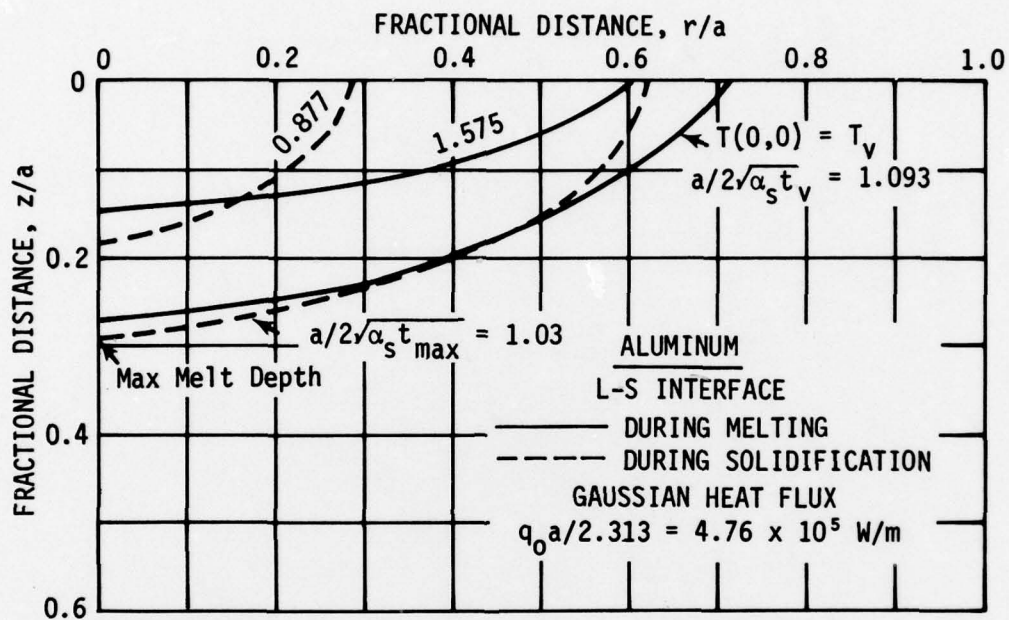


Figure 16. Liquid-solid interfaces during melting and subsequent solidification of an aluminum substrate subjected to a Gaussian absorbed heat flux distribution over a circular region of radius a .

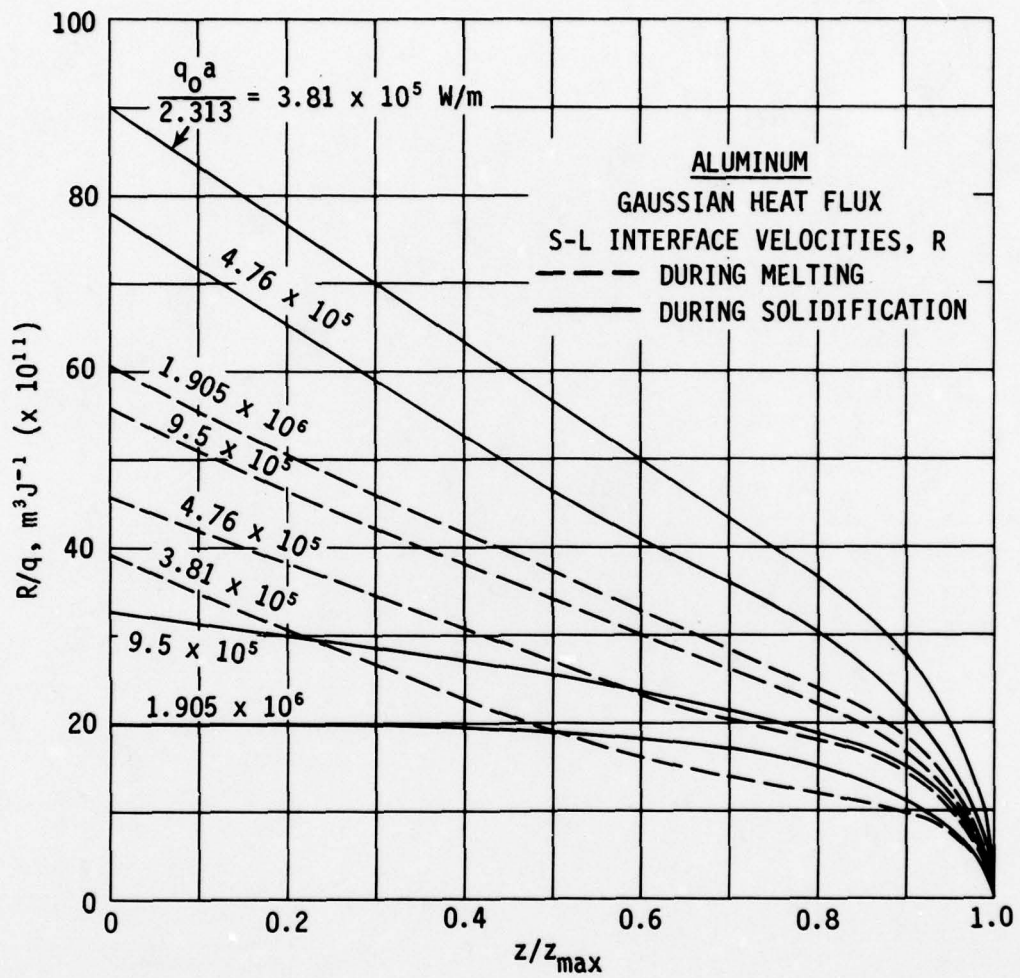


Figure 17. The ratio of liquid-solid interface velocity to absorbed heat flux as a function of fractional distance, z/z_{\max} , during melting and solidification of an aluminum substrate subjected to a Gaussian absorbed heat flux distribution over a circular region of radius a .

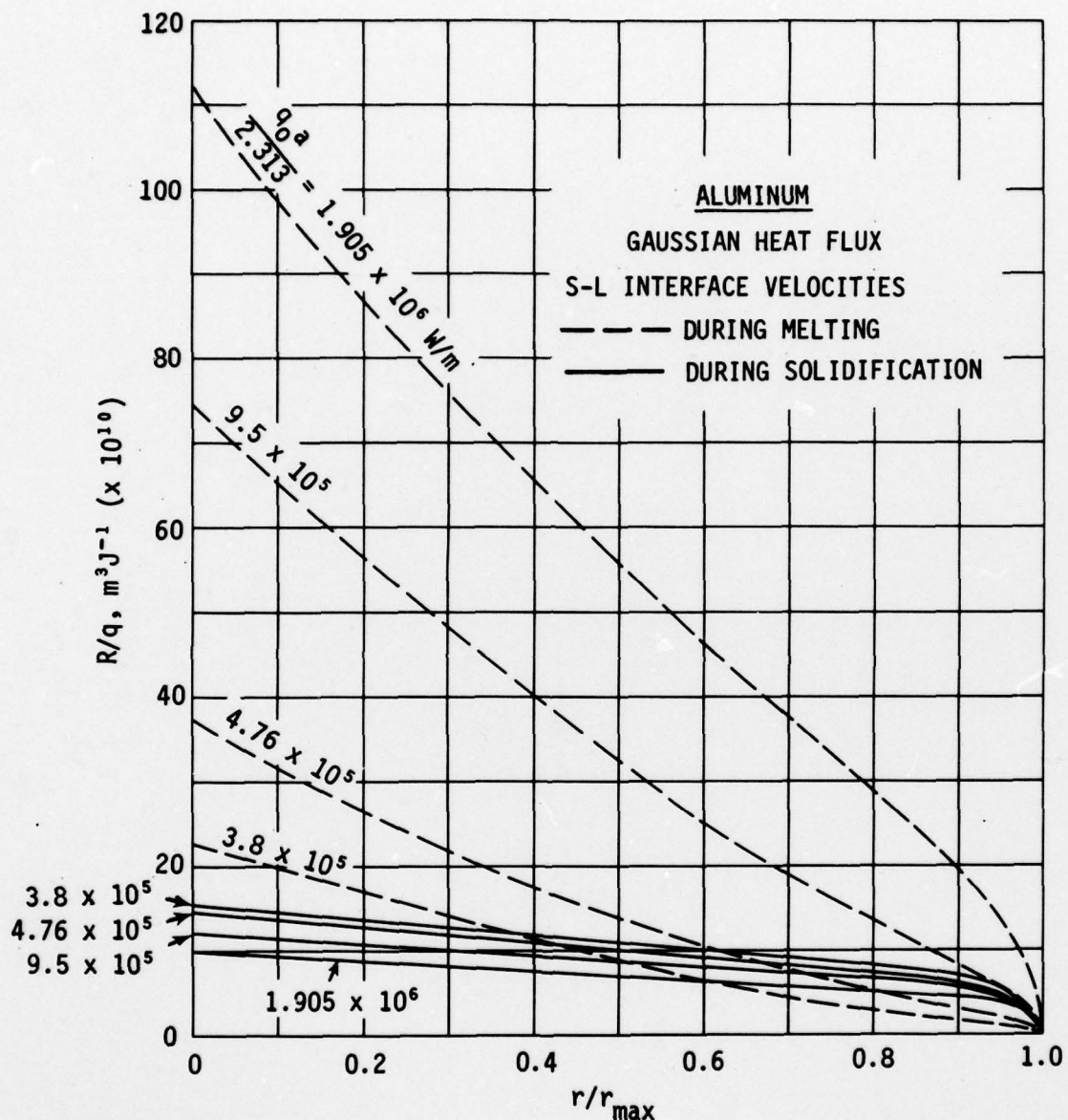


Figure 18. The ratio of liquid-solid interface velocity to absorbed heat flux as a function of fractional distance, r/r_{\max} , during melting and solidification of an aluminum substrate subjected to a Gaussian absorbed heat flux over a circular region of radius a .